Spring 2020

Slip rates and kinematics of active crustal faults in the central Oregon Cascades

Katherine Alexander
Western Washington University, katiealexander21@gmail.com

Slip rates and kinematics of active crustal faults in the central Oregon Cascades

By

Katherine A. Alexander

Accepted in Partial Completion
of the Requirements for the Degree
Master of Science

ADVISORY COMMITTEE

Dr. Colin B. Amos, Chair

Dr. Douglas H. Clark

Dr. Andrew J. Meigs

GRADUATE SCHOOL

David L. Patrick, Interim Dean

Master's Thesis

In presenting this thesis in partial fulfillment of the requirements for a master's degree at Western Washington University, I grant to Western Washington University the non-exclusive royalty-free right to archive, reproduce, distribute, and display the thesis in any and all forms, including electronic format, via any digital library mechanisms maintained by WWU.

I represent and warrant this is my original work, and does not infringe or violate any rights of others. I warrant that I have obtained written permissions from the owner of any third party copyrighted material included in these files.

I acknowledge that I retain ownership rights to the copyright of this work, including but not limited to the right to use all or part of this work in future works, such as articles or books.

Library users are granted permission for individual, research and non-commercial reproduction of this work for educational purposes only. Any further digital posting of this document requires specific permission from the author.

Any copying or publication of this thesis for commercial purposes, or for financial gain, is not allowed without my written permission.

Katherine Alexander

4/10/2020

Slip rates and kinematics of active crustal faults in the central Oregon Cascades

A Thesis
Presented to
The Faculty of
Western Washington University

In Partial Fulfillment
Of the Requirements for the Degree
Master of Science

by
Katherine A. Alexander
April 2020

Abstract

New cosmogenic ^{3}He chronologies and surficial geologic mapping constrain the age of glacial deposits and slip rates of predominantly normal faults in the White Branch and Dilman Meadows fault zones in central Oregon, USA, over the last ca. ~80 kyr. Our mapping of glacial landforms and deposits distinguishes three primary episodes of glacial deposition in the White Branch fault zone. Twenty-two new cosmogenic ^{3}He surface exposure dates indicate that the youngest glacial unit represents a last glacial maximum deposit (ca. 19.4 +10.1/-6.2 kyr). Mapping of outwash terrace surfaces and deposits in the Dilman Meadows fault zone, constrained by two new cosmogenic ^{3}He depth profiles, identifies an older outwash deposit (75.0 +11.3/-9.2 kyr) associated with MIS 5b (~75 ka), as well as a younger last glacial maximum outwash surface (20.8 +0.04/-0.03 kyr). For the first time, glacial chronologies are linked across the Cascades, where west of the crest, where erosion and precipitation rates are high and vegetation cover is dense, and east of the crest, where precipitation and erosion rates are significantly lower and tree cover is sparse. We use offset measurements from fault scarps that show primarily dip-slip motion in combination with the depth profile ages to determine a summed slip rate across the Dilman Meadows fault zone of 0.1 – 0.4 mm/yr since ~75 ka. Surface faulting evident in the White Branch fault zone represents deformation strictly since the last glacial maximum (< 20.3 +6.2/-5.3 ka). Combining offset values from scarp profiles that show purely dip-slip displacement with the cosmogenic ^{3}He surface ages yields a summed dip slip rate across the White Branch fault zone of 0.6 ± 0.5 mm/yr since the last glacial maximum. The White Branch and the Dilman Meadows fault zone both accommodate mostly extension in the Cascade arc and could be mechanisms of Siletzia rotation or volcanic upwelling.

Acknowledgements

This research was supported by funding from the Western Washington University Graduate School, and the Western Washington University Geology department. All lidar DEMs used for mapping and topographic analysis were obtained from the Oregon Department of Geology and Mineral Industries. To all those that helped me with this work, Willy Amidon and Reyne Lesnau at Middlebury College, Greg Balco at the Berkeley Geo Chronology Center, I learned so much from all of you.

I want to thank everyone in the geology department for their support during my time at western, –Ben Paulsen for everything you do for the students and our projects, Kate Blizzard for answering my endless questions, and Paul for always checking in.

To my cohort, we lucked out. Lexi, Liza, and Paige, I will always be so happy that we got to go through this together ! Cody, thank God you were here and willing to dive into every Thursday afternoon caffeine driven rabbit hole that would lead to nowhere. I miss your fried chicken.

To my new fiends in Bellingham, boating, biking, foraging, and exploring would not have been the same or even possible without you. Thanks to people of the Bike House for welcoming me in with open arms, Avery and Nyle you are the first real roommates I have ever had and I couldn't have ask for better fiends out of all of this.

Nolan thanks for taking me on all the adventures, making me dinner, and sticking with me through all of this.

My family, Mom, Dad, Mimi, Jos, Rick, Gary, Johnathon, Chris, Nuts, Lil P, and Chugs (in no particular order). Mom and Dad I can't believe you actually bush-wacked through central Oregon looking for boulders with me, thanks for being a constant source of amusement. Mimi and Rick, thanks for always answering when I call, love you. Jos and Gary, thank you for teaching me about colors and telling me to stay in school, love you.

Finally, I want to thank my committee for sticking with me and making me a better scientist. Doug without your advice my maps would not be as they are today. Andrew, I don't even know what to say. You helped get me here and I am so grateful for all the opportunities and advice that have helped me get to where I am today. Colin, I have loved this project from start to finish and you have taught me how to work independently while also always being there. I am extremely happy that we were able to work on this project and all our other side projects together. #MyAdvisorsAreTheBestAndIAmGoingToMissThis

Table of Contents

List of Tables and Figures

Introduction

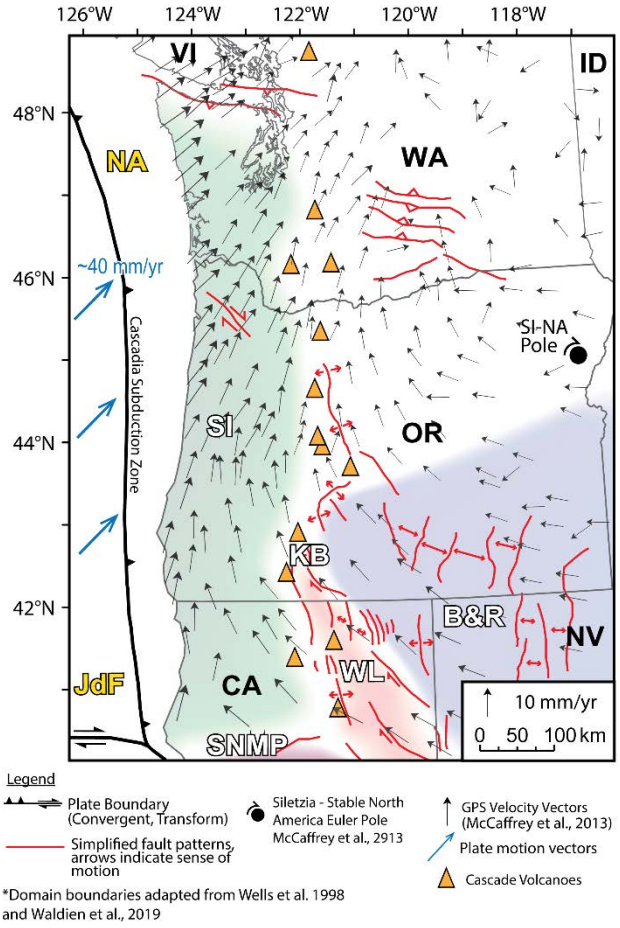

Figure 1: Tectonic overview of western North America. GPS surface velocities (black arrows) corrected for Cascadia subduction zone coupling from McCaffrey et al. (2013). Orange triangles show major volcanoes in the Cascade Range. Red lines show simplified pattern of Quaternary faulting adapted from the US Geological Survey (2006). Colored areas show general domains of the Pacific Northwest. OC-NA Pole is the Siletzia pole of rotation relative to North America from Wells et al. (1998). SI = Siletzia, B&R = Basin and Range, WL = Walker Lane, SNMP = Sierra Nevada microplate, NA = North American Plate, PAC = Pacific Plate, OR = Oregon, ID = Idaho, WA = Washington, CA = California, NV = Nevada, VI = Vancouver Island.

Crustal faults in the Pacific Northwest of the United States of America accommodate both long and short-term deformation reflecting interactions of crustal blocks delineated by both geology and geodesy (Figure 1) (Wells et al., 1998). Long-term deformation evidenced by paleomagnetic rotations reveals relatively continuous clockwise rotation since the Neogene of the Oregon forearc with respect to stable North America about a pole near the Washington Oregon Idaho Border (Simpson and Cox, 1977; Wells and Heller, 1988; McCaffrey et al., 2007). Short-term deformation revealed by geodesy paints a similar picture of clockwise rotation (Figure 1) (Miller et al., 2001; Hammond, 2005; McCaffrey et al., 2013), suggesting longevity of this velocity field and deformation pattern. Seismogenic crustal faults link these long and short term strain regimes by accommodating deformation accruing during repeated earthquakes cycles over millennia (Pezzopane and Weldon, 1993). Despite this crucial link, some areas of the Pacific Northwest see few geologic constraints on Quaternary-active faults owing to widespread and

often dense tree cover and nearly ubiquitous young volcanic lavas from the Cascade volcanic arc. Understanding how deformation manifests on individual active faults, the majority of which remain uncharacterized in terms of slip rate, kinematics, and earthquake recurrence could help resolve the relative role of volcanism vs. faulting in accommodating intra-arc extension (e.g., Pezzopane and Weldon, 1993; Brocher et al., 2017). Fundamentally, our understanding of the controls on active deformation in the central Oregon Cascades relies on elucidating how active faults accommodate distributed clockwise shear along the North American margin. This clockwise motion results in dextral shear and oblique, N-NW-directed extension along the eastern boundary of the Siletzia domain (Figure 1) (Waldien et al., 2019).

The understanding of the active deformation in the central Oregon region is progressing due to the rapidly expanding coverage of lidar. This coverage has changed the way we are able to study active faults, particularly in Oregon where high-resolution lidar has been acquired for nearly half of the state. Advances in cosmogenic ^{3}He exposure dating of landforms sourced from volcanic bedrock (Amidon and Farley, 2011) have led to new numerical chronologies in central Oregon (Deligne et al., 2016; Speth et al., 2018; Bacon and Robinson, 2019). As such, the Central Oregon Cascades is well suited to assess the relative role of active extensional faulting in a zone of active volcanism and glaciated terrains.

This study focuses on two fault zones that span the crest of the High Cascade volcanic arc (Figure 2). The White Branch fault zone located on the west side of the High Cascade arc axis and the Dilman Meadows fault zone located within the arc in the La Pine graben. Both sites provide the opportunity to study how extension is accommodated on fault zones within the arc. This study relies on surficial geologic mapping of fault scarps and offset Quaternary landforms using lidar-based datasets from the Department of Geology and Mineral Industries (DOGAMI)

(https://www.oregongeology.org/lidar/). Additionally, we develop a new absolute chronology based on cosmogenic dating of ^{3}He and for the first time quantitatively link the timing of glacial events on the humid, densely forested west side of the Cascade crest to those on the arid, desert landscape in the rain shadow to the east.

Background

Regional Tectonics

Crustal deformation in the Pacific Northwest is generally driven by the oblique subduction of the Juan de Fuca plate beneath the North American plate and dextral shear across the Pacific North American plate boundary (Pezzopane and Weldon, 1993). This overall plate boundary setting results in Basin and Range extension, and north directed right-lateral shear translated through the Walker Lane (England and Wells, 1991; McCaffrey et al., 2013). In the Pacific Northwest the Cascade volcanic arc generally defines the western boundary of the basin and range in Oregon and the eastern boundary of the forearc (Figure 2) (Scarberry et al., 2010; Waldien et al., 2019).

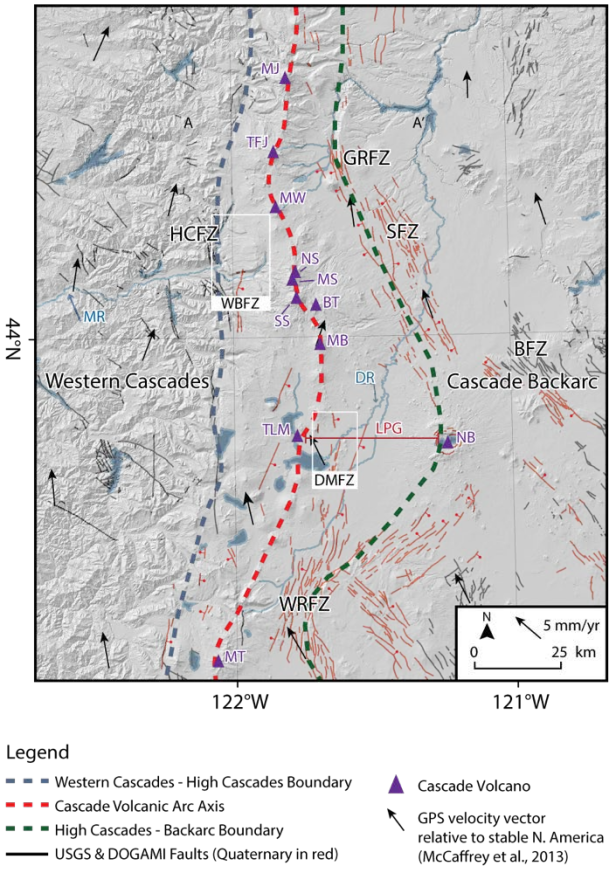

Figure 2: Central Oregon High Cascades. Dashed lines denote regional boundaries. GPS surface velocities (black arrows) corrected for Cascadia subduction zone coupling from McCaffrey et al. (2013). Black labels show major fault zones in the area. Red labels show major graben structures in the area. Purple triangles are major volcanoes. Black lines are Quaternary faults from the US Geological Survey (2006) and DOGAMI. Study areas for this project are shown in white boxes. Base layer is a lidar hillshade. GRFZ = Green Ridge fault zone, SFZ = Sisters fault zone, HCFZ = Horse Creek fault zone, BFZ = Brothers fault zone, WRFZ = Walker Ridge fault zone, WBFZ = White Branch fault zone, DMFZ = Dilman Meadows fault zone, MJ = Mt. Jefferson, TFJ = Three Fingered Jack, MW = Mt. Washington, NS = North Sister, MS = Middle Sister, SS = South Sister, BT = Broken Top, MB = Mt. Bachelor, TLM = Twin Lake Maars, MT = Mt. Thielsen, NB = Newberry Volcano, MR = McKenzie river, DR = Deschutes River.

Based on both long and short- term deformation patterns, the forearc is partitioned into large crustal domains (Wells et al., 1998; McCaffrey et al., 2013; Savage and Wells, 2015). Horizontal GPS data indicate a vertical rotation axis near the Washington-Oregon-Idaho border shown in Figure 1; conversely, the geometries of mapped strike-slip faults and GPS surface velocities suggest a vertical axis of rotation in eastern Oregon for the Siletzia domain (McCaffrey et al., 2007). The combination of paleomagnetic data and GPS data suggest Siletzia rotation has remained consistent for the last 10-16 Ma (Wells et al., 1998; McCaffrey et al., 2007; Brocher et al., 2017).

Regional Geology

The central Oregon segment of the Cascade Arc can be divided into two physiographic and geologic "domains" on either side of the roughly north-south trending arc axis (Figure 2). The West Cascades province was the active volcanic arc from 5 – 35 Ma until Basin and Range extension and rotation of the forearc caused a relative eastward migration of volcanism (Priest, 1990; Taylor, 1990; du Bray and John, 2011). Orographic precipitation of moist westerlies drives average yearly precipitation values of ~190 cm per year along the western topographic slopes, allowing for dense pine, hemlock, and fir forests. In contrast, the east side receives < 30 cm of rainfall annually, resulting in open forests of large predominantly ponderosa pine (https://www.ncdc.noaa.gov/climatenormals/clim60/states/Clim_OR_01.pdf).

From Mt. Hood south to the Klamath Graben the High Cascades are bound by fault zones that likely accommodate the rotation of the Siletzia domain (Brocher et al., 2017). At the latitude of the Central High Cascades, the Siletzia domain moves parallel to the arc relative to the backarc, and it is predicted from the velocity field that a significant component of right lateral strike-slip (0.7 -1.1 mm/yr) should be accommodated by crustal faults (McCaffrey et al., 2007)

(Figure 2). The east dipping Horse Creek fault zone bounds the High Cascades west of North Sister volcano and shows predominantly normal motion offsetting Pliocene – Pleistocene lava flows. The Green Ridge fault zone bounds the High Cascades east of Mount Jefferson and displays down-to-the-west normal motion with less offset than the Horse Creek fault (Keach et al., 1989). Both fault zones are likely the edges of normal-faulted blocks that accommodated the extension during the formation of the High Cascades (Keach et al., 1989). The Green ridge fault zone has since been offset by the northwest striking Sisters fault zone.

The Sisters fault zone extends ~ 60 km southeast from the southern extent of the Green Ridge fault zone. Initiation of the Sisters fault zone likely began in the last ~ 100 – 200 kyr and comprises dextral oblique normal faults with extension rates up to 0.5 mm/yr (Mark-Moser, 2018). On its southwestern flank some of Newberry volcanos earliest flows are offset by faults of the Walker Rim fault zone. Taylor (1981) and MacLeod and Sherrod (1988) suggested that the Walker Rim fault zone is the continuation of the northwest trending Sisters fault zone that has be deflected by Newberry volcano to a southwest trending fault zone. Newberry volcano marks the eastern extent of the La Pine Graben a structural low that has been described as the boundary between the High Cascades and the Basin and Range province (MacLeod and Sherrod, 1992).

The surficial geology of the La Pine graben, much like the High Cascades to the north, is dominated by Quaternary volcanism. Gravity data were originally used to identify the La Pine Graben as a composite graben separated by a horst referred to as the Pringle butte volcanic chain made up of a north-east trending array of buttes (Couch et al., 1982): the Wickiup (~ 0.61 Ma), Wampus, Pringle, Eaton (3.68 ± 3.3 Ma; Fiebelkorn et al., 1983), and Gilchrist (0.61 Ma; MacLeod and Sherrod, 1992). The La Pine basin is east of the horst separating the La Pine Graben, and the Shukash basin is to the west (Figure 2). Reversely polarized lava defines the

Shukash basin floor indicating the graben fill sequence is younger than 0.73 Ma (Couch and Foote 1985). Lake development and lacustrine sedimentation in the La Pine graben is evidenced by 250 m of fill seen in seismic reflection data from the Shukash Basin and in outcrops along the Deschutes River (Lyon, 2001). Two interbedded ash layers have been identified in the deposits of the Shukash basin, the Dibekulewe ash bed (500 ka; Sarna-Wojcicki et al., 1993) and the Pringle Falls D ash bed (218 ka, Herrero-Bervera et al., 1994), which may have blocked the ancestral Deschutes River causing lake formation (Lyon 2001). The Mazama tephra deposit (7,682 – 7,584 cal yr. B.P., Egan et al., 2015) mantles the Shukash Basin but is commonly only mapped where it is thicker than 1 m (Scott and Gardener, 1992). North-south trends of volcanic chains and fissures are recognized surrounding the La Pine graben (Pezzopane and Weldon, 1993; Ake et al., 2001; Personius, 2002; Weldon et al., 2003; Vadman and Bemis, 2019). The orientations of the volcanic chains are similar to known Quaternary faults in the La Pine Graben and surrounding areas.

The Wampus fault zone is the most prominent fault zone in the La Pine Graben, the N10-15°E striking 15 km long fault zone includes the Dilman Meadows fault (Lyon, 2001). The Dilman Meadows fault is a 12 km long down to the east normal fault that is well exposed in a cut bank of the Deschutes River. Previous work on the Dilman Meadows fault suggests variable slip rates since ~140 ka ranging from 0.04 to 0.15 mm/yr (Lyon, 2001). Vadman and Bemis (2019) identified several other normal fault strands that rupture the surface (<1.5 m) across the Shukash basin during reconnaissance mapping using airborne lidar. To determine the relative ages of Quaternary volcanic units that have been offset by faults surface morphologies can be compared as well as degree of erosion (Sherrod et al., 2004). In the central Oregon Cascades, however, the effects of multiple glacial cycles and deposition of Mazama tephra have made understanding the

timing of events in the area more challenging due to erosion of volcanic units and deposition of glacial units.

Glacial History

Local glaciers on individual volcanoes, as well as composite ice caps that spanned portions of the central Oregon Cascades divide resulted in substantial glacial erosion and sculpting as well as deposition. On the eastern flanks of the High Cascades from Mt. Jefferson to Mt. Washington, deposits and landforms associated with three major Quaternary glaciations are recognized: 1) the Abbot Butte Formation, 2) the Jack Creek Formation, 3) Cabot Creek Formation (Scott, 1977). The Cabot Creek Formation, the youngest of the three, comprises three distinct members: 1) the Suttle Lake Member, 2) the Canyon Creek Member, and 3) the Jefferson Park Member. Moraines associated with glaciers from the Suttle Lake Member have relatively sharp moraine crests that crosscut and bury moraines of older advances. The Suttle Lake Member of the Cabot Creek Formation correlates with the Waban drift in southern Oregon and is recognized as the last glacial maximum (LGM, ~18 -22 ka) in Central Oregon (Scott, 1977). Recent ^{3}He exposure dating record the onset of LGM deglaciation in the Klamath basin (Figure 1) of 16 - 20 ka (Speth et al., 2018). Moraine crests associated with the Jack Creek Member are more rounded than those associated with Suttle lake Member, reflecting greater post-glacial erosion and longer exposure times. The Jack Creek Member correlates with the Hayden Creek at Mt. Rainier (40 - 80 ka; Crandell and Miller, 1974), and possibly an intermediate age glacial deposit in the Klamath basin (97.6 ± 12.7 ka, Speth et al., 2018). The oldest glaciation identified by Scott (1977), the Abbot Butte Formation, does not contain any preserved moraines and where till is observed it is highly weathered with thick (several meters) of soil formation. The Abbot Butte Formation is loosely estimated at 200 – 900 ka based on soil development, weathering rind thickness on clasts in

deposits, and lack of moraine crest preservation (Scott and Gardener, 1992; Lyon, 2001; Sherrod et al., 2004) across the High Cascades from Mt. Jefferson south to the La Pine graben. The Abbot Butte Formation is included in the marine isotope stage (MIS) 6 glaciation (ca. 30-150 ka, Lisiecki and Raymo, 2005), other possible MIS 6 glacial deposits (168.9 ± 22.3 ka) are recognized in the Klamath basin as well (Speth et al., 2018).

In the central High Cascades, till of Suttle Lake (LGM) stade within the Cabot Creek glaciation is inset within till from the Jack Creek glaciation, based on mapping by Sherrod et al., (2004). Two major outwash surfaces graded to moraines occur in the Shukash basin, the western sub-basin of the La Pine graben (Figure 2) (Scott and Gardener, 1992). Both surfaces are mantled with Mazama tephra, and geophysical evidence from a survey completed by the Bureau of Reclamation (BOR) (Miller and Markiewic, 2000) suggests there is yet an older outwash surface interbedded within the lacustrine deposits (Lyon, 2001). The deposit imaged in the BOR seismic reflection survey (2002) was not sampled but was proposed to be from a glaciation older than Jack Creek based on surficial mapping by Scott (1977) (Lyon, 2001).

Surficial geologic mapping

Analyzing new, high-resolution airborne bare-earth lidar from DOGAMI using Quick Terrain Modeler and ESRI ArcGIS, we mapped volcanic and surficial deposits, offset geomorphic markers (e.g., glacial moraines and both aggregational and degradational fluvial terraces), and fault traces, which in turn guided our field mapping and sample collection (https://www.oregongeology.org/lidar/). Our mapping of the White Branch fault zone distinguishes the relative ages of glacial deposits based on the positions of the moraines in the landscape, the preservation of the original hummocky topography, and moraine crest sharpness,

as imaged in the lidar data. In the Dilman Meadows fault zone, we use the lidar data not only to create a surficial geologic map, but also to compare the elevations of terrace treads to create a terrace map parallel to the Deschutes River. Fieldwork focused on qualitatively assessing the relative boulder frequencies in glacial units in the White Branch fault zone and relative stratigraphy of glacial deposits and Mazama tephra deposits in the Shukash Basin.

White Branch fault zone

High resolution airborne bare-earth lidar presents the opportunity to identify displaced and datable Quaternary geomorphic surfaces cut by surface rupturing faults that are obscured by dense forest cover and young arc volcanism. Mapped portions of the White Branch fault zone used all available lidar in this vicinity, with the map area encompassing the eastern boundary of the West Cascades to the western slopes of the High Cascade crest for a total mapped area of 750 km^2 (Figure 3a and Plate 1). Using bare-earth lidar data, Quick Terrain Modeler and its surface elevation profiling tool, and ESRI ArcGIS, we mapped at a 1:8,000 scale identifying volcanic and geomorphic deposits, offset geomorphic markers (e.g., moraines), and fault traces. Younger glacial deposits are preserved at higher elevations and on valley floors and they qualitatively appeared to have higher boulder frequencies and sharper crests than older moraines. The younger surfaces have remained relatively unchanged since glaciers receded (Scott, 1977, Speth et al., 2018). Our glacial deposit mapping builds on work completed by Scott (1977) east of Three Fingered Jack (Figure 2), as well as previous bedrock mapping (Black et al., 1988; Walker and Duncan, 1989; Sherrod et al., 2004; Deligne et al., 2016).

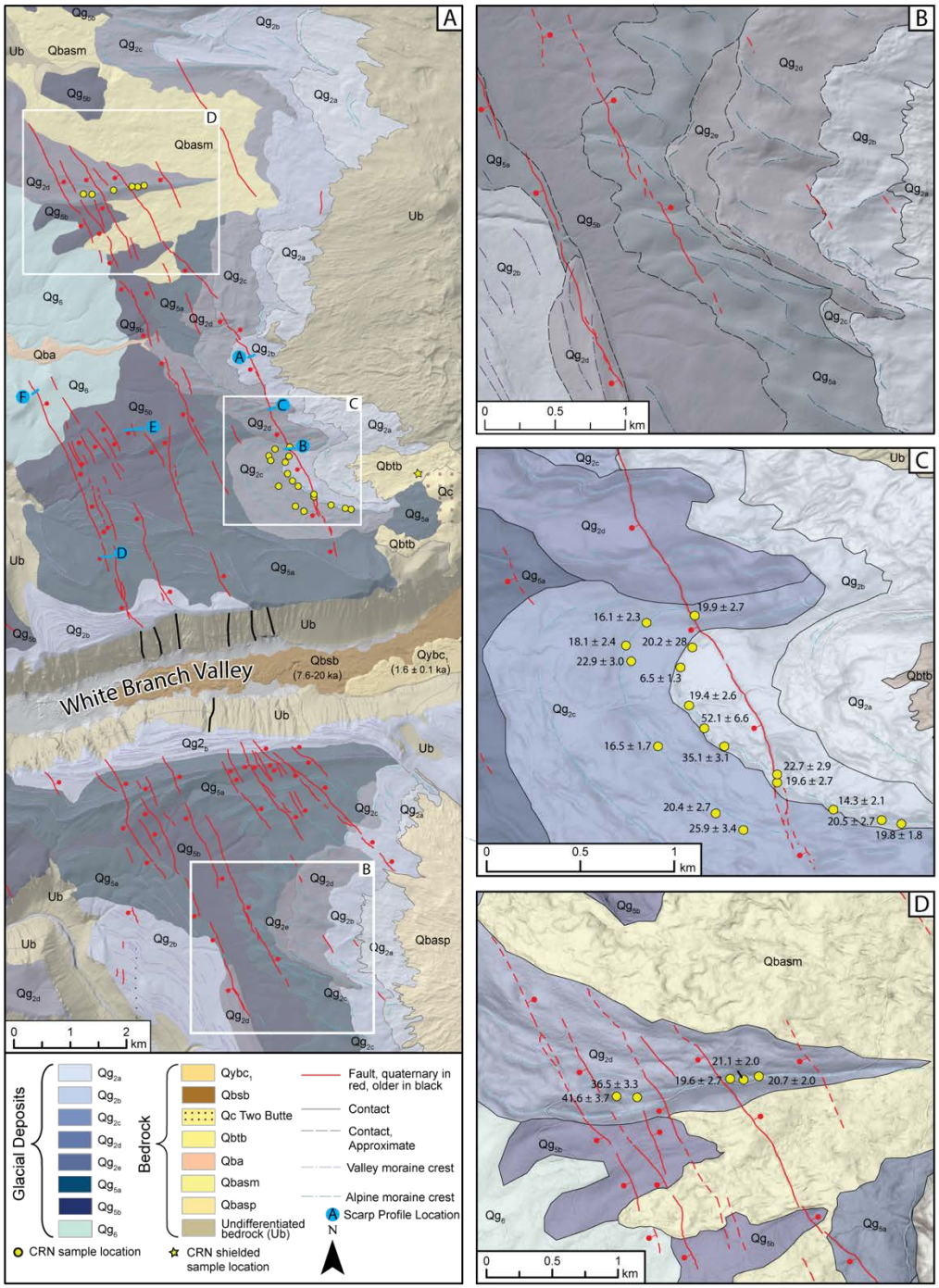

Figure 3: (A) Surficial geologic map of White Branch fault zone, Oregon, USA, over lidar bare earth hillshade available from the Department of Geology and Mineral Industries. Full map can be found in Supplementary S1-2. Bedrock mapping is a compilation of several published geologic maps (Preist et al., 1988, Walker and Duncan, 1989, Sherrod et al., 2004, Walker and MacLeod, 1991, Hildreth et al., 2012, Deligne et al., 2016). Unit descriptions are included with S1 in supplementary material. (B)Surficial map showing cross cutting relationships of moraines from multiple glacial deposits. (C) Surficial map of terminal moraines in Last Glacial maximum age deposits, ^{3}He boulder sample locations shown with ages reported in ka (± 1σ). (D) Surficial Geologic map of glacial deposits, specifically lateral moraine in Qg_{2d} surrounded by younger volcanic deposits. ^{3}He boulder sample locations shown with ages reported in ka (± 1σ).

Three generations of glacial deposits and landforms are recognized in the White Branch fault zone (Qg_2, Qg_5, Qg_6). Throughout the fault zone, we distinguish between valley glacier moraine crests and alpine moraine crests, where alpine crests are preserved from smaller glaciers at higher elevations and valley moraine crests are the result of glaciers in the White Branch Valley that exceeded the height of the valley walls depositing material laterally (Figure 3a). The oldest glacial deposits (Qg_6) are preserved only at the lowest elevations other than the valley floors, in the northwest extent of the mapping area. These deposits are distinguished from younger glacial deposits by the northeast – southwest glacial fluting of the landscape, the lack of preserved moraine crests, lack of any large boulders on the surface, and by a thicker soil formation on the surface of up to ~3 m (Supplementary S3). The contact between Qg_6 and Qg_5 is approximated at the lowest elevation of moraine crest presence in Qg_5. Unit Qg_6 most likely correlates to Abbot Butte glaciation from Scott (1977).

The intermediate glacial deposit (Qg_5) is greatly affected by faulting and has well-formed crests that are distinctly more rounded than those of Qg_2. The Qg_5 moraine slopes have qualitatively gentler slopes and are less rocky compared to moraine crests seen in younger glacial deposits (Qg_2). Locating moraine boulders in the field was challenging due to dense cover by Manzanita bushes that commonly surrounded and concealed boulders. Of the boulders we were able to locate, most were highly weathered and less than 0.5 m in diameter. Road cuts into this unit reveal the surface is dominated by organic matter, and the depth of soil formation is likely variable across the unit. The intermediate deposit is subdivided into Qg_{5a} and Qg_{5b} due to cross cutting relationships of the moraine crests (Figure 3b). Based on moraine crest sharpness and position in the landscape we correlate Qg_5 deposits to the Jack Creek Formation of Scott (1977) and Sherrod et al., (2004).

The youngest glacial deposit in the White Branch Valley map area (Qg_2) consists of a suite of recessional terminal and lateral moraine sequences distinguished by sharp lateral moraine crests and hummocky topography of the terminal moraines. Boulders on the surface are slightly weathered and range in size from < 1 m in diameter to > 2 m in diameter. The relative degree of soil formation varies across the unit but is dominated by organic matter in the upper 30 cm of the ground surface. The Qg_2 unit is the only glacial deposit observed on the White Branch Valley floor and is subdivided into Qg_{2a-e} based on cross-cutting relationships of moraine crests (Figure 3b).

Previous mapping of bedrock and the younger lava flows in the area (Black et al., 1988; Walker and Duncan, 1989; Sherrod et al., 2004; Hildreth, 2007; Deligne et al., 2016) documents that the oldest bedrock units are 6.8 - 6.3 Ma basalts which are found primarily in the western half of the mapping area. Basaltic andesites ca. 0.63 ± 0.09 Ma underlie the glacial units centered in the mapping area and in some cases are distinguished from one another by source location. The basaltic andesite of Scott Mountain (Qbasm) north of the Which Branch Valley has one reported age of 35 ± 25 ka from a single $^{39}Ar/^{40}Ar$ measurement; we map this unit between two sub-units of Qg_2 therefore defining its deposition age as during the LGM (Jefferson et al., 2006). The youngest lava flows, cosmogenically dated to 2.7 – 1.5 ka, were erupted from Belknap Crater in the northwest region of the map area and overlay Qg_2 deposits (Sherrod et al., 2004).

Geologic units in the White Branch Valley area are transected by a complex and highly distributed zone of faulting ~30 km long and ~10 km wide. The faults are dominantly north-northwest striking, steeply dipping to the east and west, and are highly segmented with typical

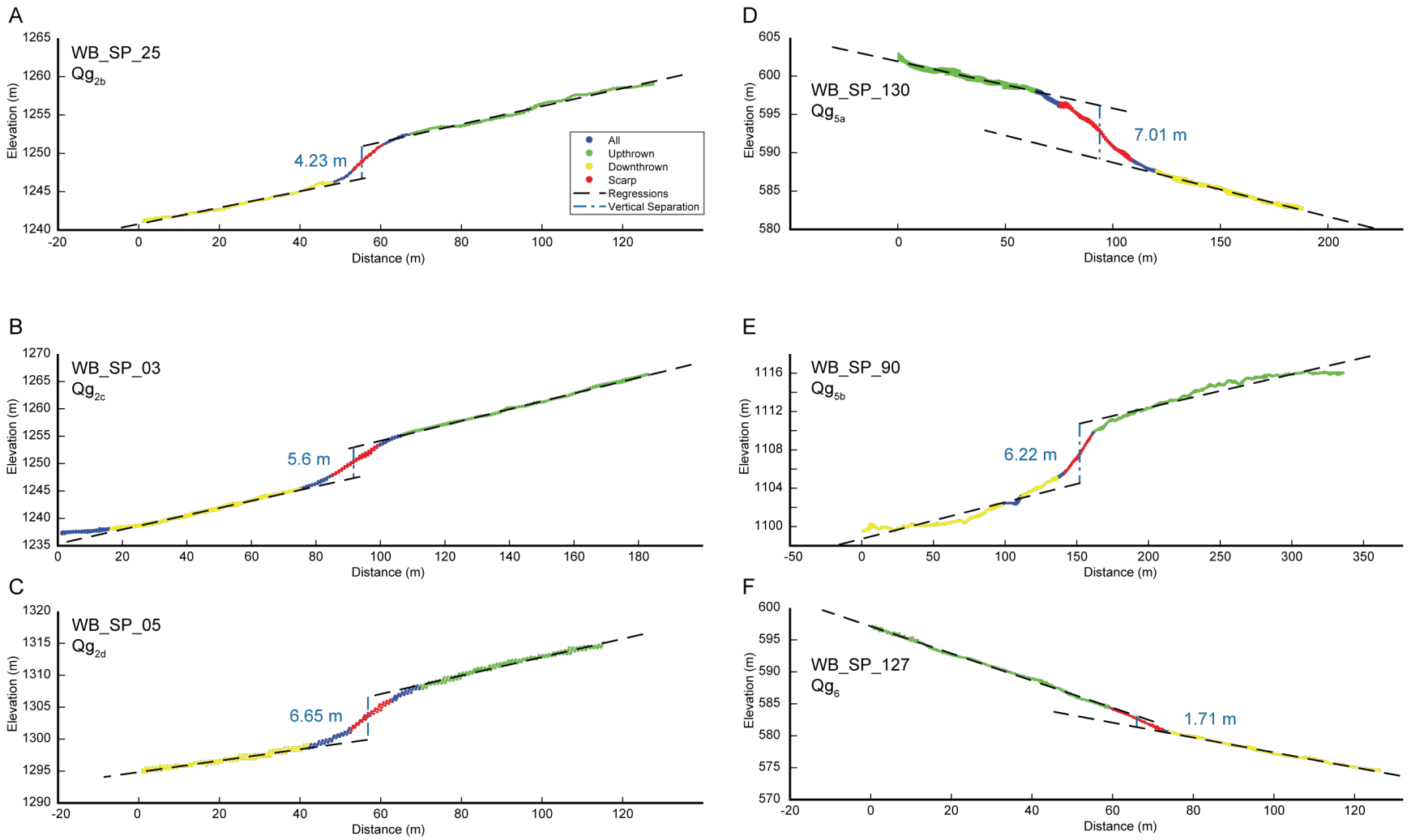

Figure 4: Example scarp profiles from each glacial deposit in the White Branch fault zone. Distance measured is from west to east. Values reported next to scarp face are median vertical separation measurements calculated using a Monte Carlo Simulation, which assumes a range of fault dips from 60 - 90 degrees. Profile letter (A-F) corresponds to Figure 3a. Legend shown in A applies to all scarp profiles.

lengths < ~2.5 km for individual fault strands. Moraine crests offset by faults show purely dip-slip separation and are used as piercing lines for fault slip calculations (Figure 3c and 3d). Scarp heights vary across the fault zone and across units (Figure 4 a-f). The fault zone comprises several small grabens that are in general right-stepping from south to north. At the northern extent the fault zone either dies out, is buried by young lava flows, or begins to change orientation and fissures are observed to strike north-northwest in glacial deposits (Figure 5a-d).

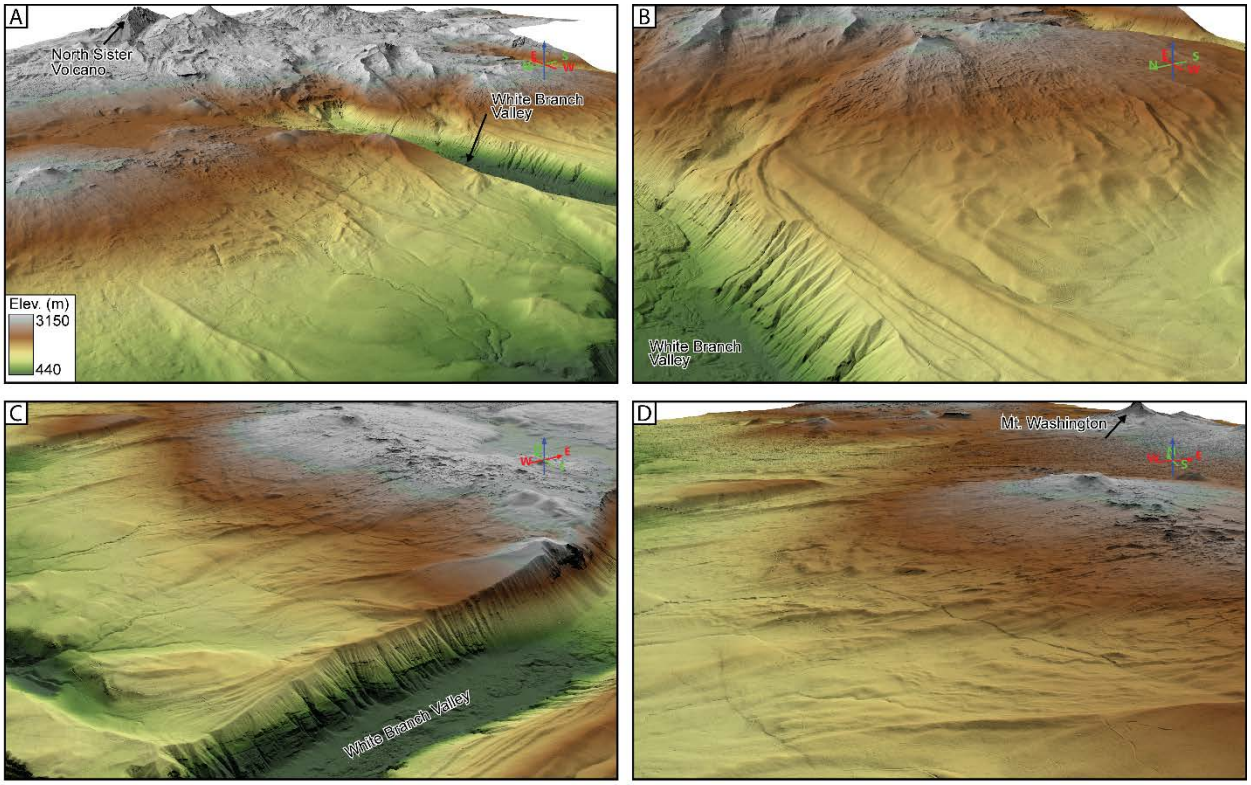

*Figure 5: (A) View looking south east at the Three Sisters volcanoes, and faults that offset glacial features on the new sloped of the volcanoes separated by the White Branch Valley. (B) View east southeast of faults south of the White Branch Valley offsetting multiple recessional lateral valley moraines and terminal alpine moraines. Lava flows from Sims Butte (1.6 ka) are visible on the valley floor. (C and D) Views northeast of faults offsetting recessional lateral valley moraines and terminal alpine moraines north of the valley. *Elevation in A applies to all images.*

Dilman Meadows fault zone

Situated in the Shukash basin, the mapped area (175 km^2) encompasses the eastern shore of the Wickiup reservoir and the northern and southern slopes of numerous volcanic cones that make up the eastern high Cascades (Figure 6a). The region is sparsely forested with Ponderosa

Pine trees that dominate this portion of the Deschutes National Forest, and unlike the White Branch fault zone, has relatively low relief and low precipitation (Figure 6b). The closest moraine deposits are located about 15 km west of the map area and were deposited by an east flowing glacier fed by ice separate from the ice that fed glaciers flowing west in the White Branch Valley. The modern Wickiup Reservoir lies between these moraines and the fault zone. Seismic reflection studies conducted within the basin show up to 250 m of fill in the Shukash basin, consisting of Quaternary glacial outwash (~ 50 m thick), Quaternary lacustrine sediments and tephra layers (~200 m) (Lyon, 2001). Lyon (2001) distinguished two glacial outwash units with thicknesses that vary laterally: Qgo_5 which is generally > 5 m thick and Qgo_2 which is 1.5 – 13.4 m thick (Figure 6c). Several cut terraces incise the younger outwash deposit along the Deschutes River. The region is blanketed by < 3 m thick tephra deposit from the eruption of Mount Mazama (7682 – 7584 cal yr. B.P; Egan et al., 2015) that occurred ~100 km to the south, with the exception of the late-Holocene fluvial terraces (T_0 and T_1) that comprise modern channel deposits and reworked Mazama tephra.

We distinguish geomorphic map units based on lidar data and lidar derivatives (slope, hillshade, relative elevation models) focusing our mapping on units covered by the tephra deposit, as well as cut-bank exposures of the modern Deschutes River (Figure 6d), and hand dug test pits (https://www.oregongeology.org/lidar/). The lidar data allowed us to refine the original bedrock mapping by MacLeod and Sherrod, (1992) and surficial mapping of Quaternary deposits by Lyon (2001). The basaltic andesite that bounds the Shukash basin to the north and south varies from Holocene to Pliocene in age, with the exception of the Wickiup Butte which is directly dated at 610 ± 5 ka (Sherrod et al., 2004).

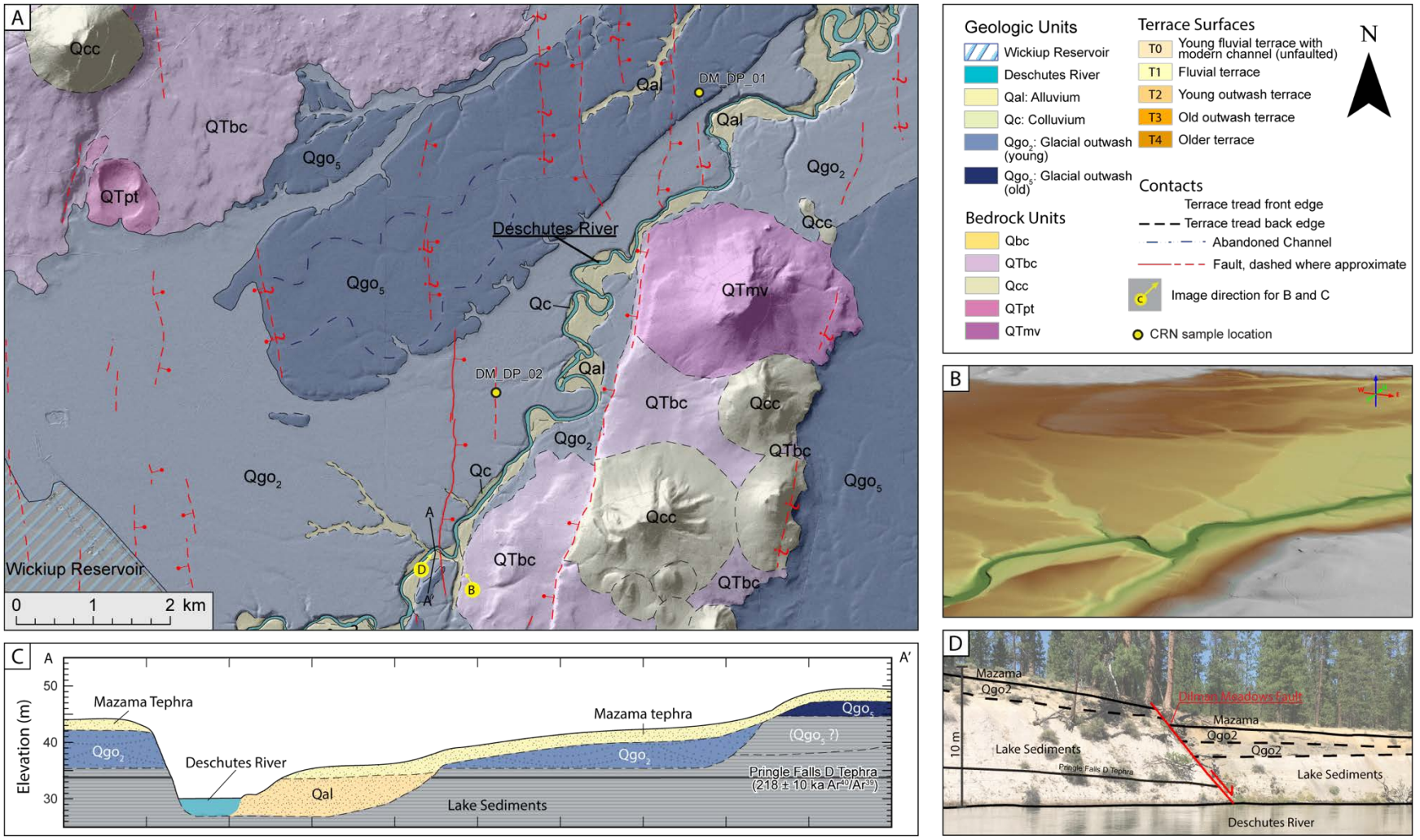

Figure 6: (A) Surficial geologic map of the Dilman Meadows fault zone. Full map can be found in supplementary S4-5 (B) 3D northwest view of the Dilman Meadows fault offsetting glacial outwash deposits from Quick Terrain Modeler. (C) Schematic cross-section A - A' shown in A. Diagram shows optional cut-in-fill terrace type for Qgo_2 in southern extent of cross section. (D) Photo of Dilman Meadows fault offset looking north from the south side of the river photo location shown in A.

The oldest outwash surface, Qgo_5, contains terrace surface T_4 and abandoned fluvial channels on its surface (Figure 6a). Post-deposition incision of Qgo_5, followed by aggradation related to the LGM created the inset Qgo_2 terrace (Lyon, 2001). Unit Qgo_5 consists of fine gravels and interbedded sand with crossbedding; a well-developed soil profile is present in the upper 60 cm. Grain sizes range from 1 mm – 5 mm in sandy layers and 1 mm – to 250 mm in sandy gravel layers. Grains are a mix of rock types but predominantly consist of basalt to basaltic andesite. Roots are present throughout the soil layer and are not observed at depth.

The most laterally extensive unit in the mapping area is the Qgo_2 outwash fill, which contains cut-in-fill terraces T_3 and T_4 (Figure 7a and b). The deposit consists of gravels and interbedded sand with roots observed to depths of 75 cm in some locations. The relative degree of soil development is less than in Qgo_5 and observed only to depths of 45 cm grading gradually to sands and gravels similar to those observed in Qgo_5.

Unit Qal is found on either side of the modern channel and in some locations contains outwash gravels, reworked Mazama tephra, alluvium, and colluvium (Lyon, 2001). The highest terrace surface in Qal is T_1 and is a fill terrace. Terrace T_0 is a cut-in -fill terrace that actively changes with water level of the Deschutes River.

The Wampus fault zone displaces the volcanic units in the southeast portion of the mapping area, which we include along with preliminary fault mapping by Vadman and Bemis (2019), and our own fault mapping to describe a zone of faulting across the Shukash Basin (Figure 6a). The faults that offset outwash units are generally north south striking unlike those that are mapped as part of the Wampus fault zone that are more northeast striking. The faults zone is ~10 km wide and contains dominantly steeply dipping normal faults that dip both to the east and west, and in some cases the dip direction changes along their length resulting in scissor like motion. Fault

segments vary in length from 0.5 km to 3 km, and where they offset terrace risers, we measure displaced piercing points for fault slip calculations. One instance of potential lateral separation is on the Dilman Meadows fault, where terrace risers appear to be right laterally offset up to 11.1 +3.4/-0.02 m making the ratio of lateral to vertical offset as large as 3:1 (Figure 7 c-d and Supplementary S6). Lateral offset measurements on the Dilman Meadows Fault are somewhat equivocal in that they include a vertical scarp, which therefore leads to uncertainties in how to project piercing lines into the fault zone.

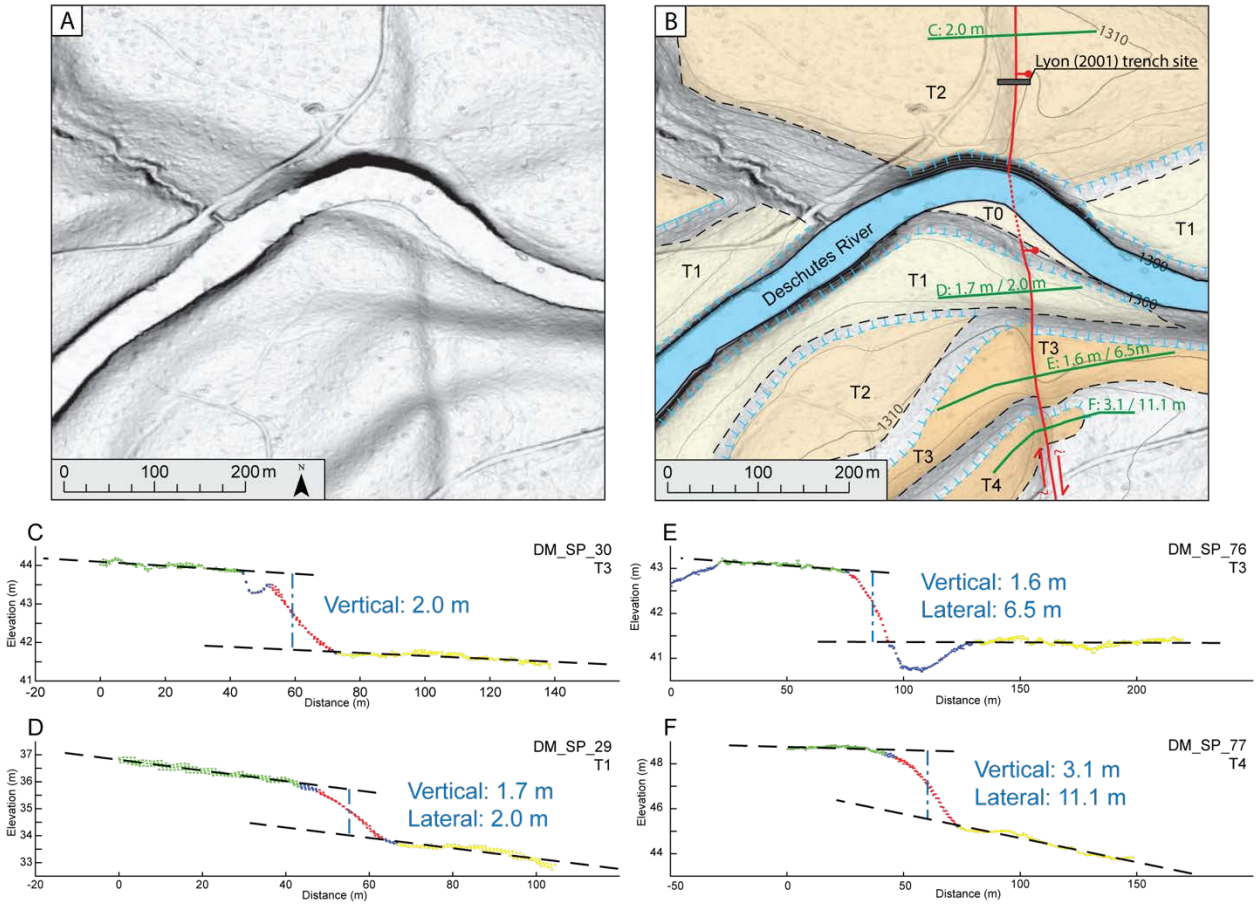

Figure 7: (A) Uninterrupted slope-shade map showing offset terrace treads near the Deschutes River. (B) Map of terrace treads offset by the Dilman Meadows fault. Profiles show locations of scarp profiles C-D. Incremental offset is observed from T1 to T4 with the exception of scarp profile E. Values reported next to profile letter are vertical offset measured / lateral offset measured.

SCARP PROFILES

By profiling fault scarps, we are able to measure displacement and quantify slip rates across the White Branch and Dilman Meadows fault zones. We use Quick Terrain Modeler v8.0.7.1 to extract 3-m wide topographic swath profiles from lidar orthogonal to fault scarps to measure the vertical displacement, dip-slip displacement, and extension. This analysis focused on geomorphic features, including moraine crests in the White Branch fault zone and terrace treads on outwash surfaces in the Shukash Basin. Following the methods of Thompson et al., (2002), we report values using a Monte Carlo approach that simulates 100,000 trials of several input parameters and uses a gaussian distribution to report the offset with the highest probability. The inputs for this simulation include: 1) linear regression slopes and intercepts of the footwall, hanging wall, and scarp face from topographic profiles from bare earth lidar derived from Quick Terrain Modeler, 2) the dip direction of the fault, 3) a range of fault dips between 60-90°, and 4) the intercept location of the fault plane along the scarp face using a trapezoidal distribution. The simulation creates probability distributions that are then used to calculate the predicted vertical separation, slip, and extension with 95% confidence intervals for a measured offset, and we report the median values with 2σ uncertainties about the median. We profiled faults where both the units and surface geometries could be reliably correlated across the fault trace. Scarp profile locations were selected based on preservation of the scarp faces and on the certainty of correlating the same geologic deposits on either side of the scarp. We chose not to profile scarps where measurements would be poor so as not to inflate our errors more than necessary (DuRoss et al., 2019). Fault dips were constrained to a range of typical normal fault dips from 60° – 90° and based on observations made from the lidar.

White Branch fault zone

We focused on profiling scarps in locations where there were moraine crests offset by faults, followed by profiling along strike of the faults to obtain as many measurements as possible. We chose not to measure in equal distance intervals, because we would have been forced to measure scarps in less than ideal locations resulting in increased measurement uncertainty. A total of 140 scarp measurements reveal broad distributions of purely dip-slip displacements (Supplementary S7-9).

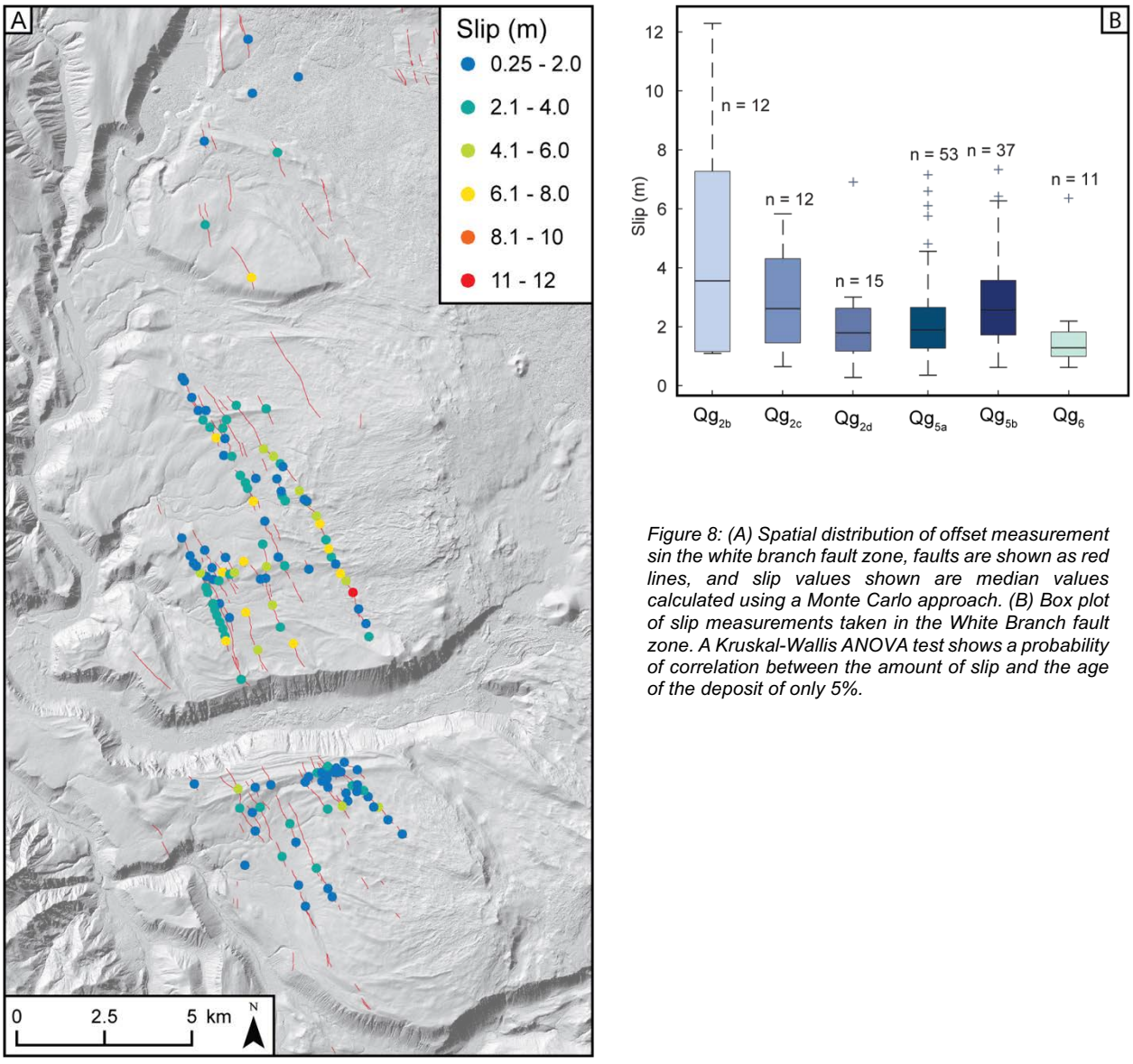

Figure 8: (A) Spatial distribution of offset measurement sin the white branch fault zone, faults are shown as red lines, and slip values shown are median values calculated using a Monte Carlo approach. (B) Box plot of slip measurements taken in the White Branch fault zone. A Kruskal-Wallis ANOVA test shows a probability of correlation between the amount of slip and the age of the deposit of only 5%.

Fault scarp profiles from offset glacial deposits in unit Qg_{2a-e}, Qg_{5a-b}, and Qg_6 show slip values ranging from 0.3 – 12.7 m, 0.3 – 7.6 m, and 0.4 – 6.6 m respectively (Figure 8a). There does not appear to be a correlation between the age of the deposit and the amount of measured offset; even the largest offsets in the oldest unit (Qg_6) are within the mean of the offsets observed in the youngest unit. This observation is supported by a Kruskal-Wallis ANOVA test χ^2 value of 0.05 (Figure 8b)

Fault strands are highly segmented and show variable displacement measurements along strike; however, when all vertical separation measurements are compared individually in a normal kernel density estimate, two populations stand out (Figure 9). The first population includes vertical separation measurements 0 – 4.5 m which includes 85% of all measurements, and the second population of vertical separation measurements 1.9 m – 12.3 m which includes 50% of all measurements. We are able to compare the vertical separation populations along strike of the fault zone by calculating the mean average vertical separation using a 1 km moving

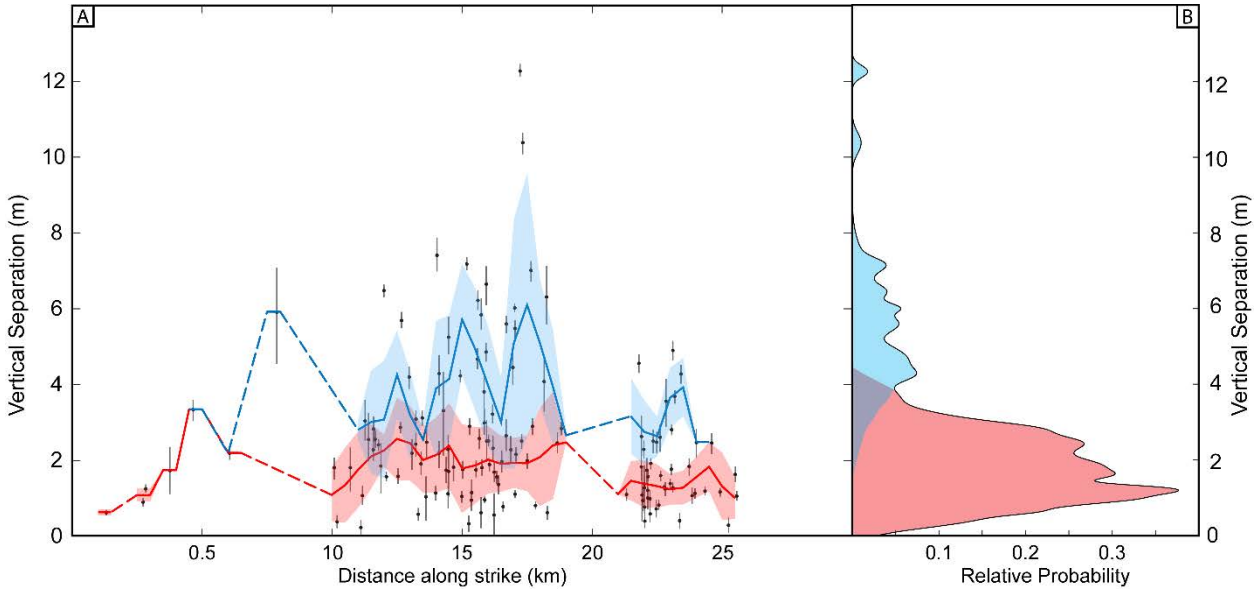

Figure 9: (A) 1 km moving average of most recent earthquake (MRE) population plotted with the older earthquake population in the along strike direction from north to south (27 km). Error windows are 1σ and gaps in section are regions where no offset measurements were collected. (B) Probability distribution of all vertical separation measurements using 1σ errors. We interpret two populations of vertical separation population 1) 0 - 4.45 m of vertical separation from the MRE and an older population with offset values greater than 1.86 m which would be the result of earthquakes that occurred prior to the MRE.

window with a 2σ error envelope (Figure 9a). Gaps (dashed lines) in the along-strike profile represent areas where there were no piercing points in offset features that we were able to measure. From north to south the differences in populations become apparent especially from 11 to 18 km where the difference between populations is greatest (Figure 9a). This relationship is also apparent in map view where measurements that contribute to each population are broadly distributed across the fault zone (Figure 8). Beyond the northern- and southern-most scarp profiles, the fault zone either dies out, is buried by relatively young lava flows, or cannot be identified due to gaps in the lidar coverage.

Dilman Meadows Fault Zone

Scarp profiles measured in the Dilman Meadows fault zone are partially obscured by the Mazama cover, resulting in more uncertainty for each measurement. Of the offset measurements collected we infer that below the tephra, the glacial units have similar displacements to those observed on the surface. We recognize that diffusion of the Mazama tephra across the scarp could decrease the measurement, but consider the effects of this process to be relatively minimal. The nature of the tephra deposit is also a source for minimizing the amount of offset recorded on fault scarp in the near field, where loose unconsolidated tephra diffuses rapidly across topographic scarps relative to outwash deposits.

Displacement measurements from 120 scarp profiles (Supplementary S10-12) reveal predominantly dip-slip motion with slip values ranging from 0.3 – 5.3 m. Displacement patterns on individual faults in the Dilman Meadows fault zone are similar to those in the White Branch fault zone in that they are highly segmented and are variable across geologic units, but there is a slight increase in offset from Qgo_2 to Qgo_5 (Figure 10). For the Dilman Meadows fault however,

offset values are largest near the center of the main trace and tail off towards either end (Supplementary S13).

We measure terrace risers that have potential for lateral offset caused by earthquakes on the Dilman Meadows fault, where we have also measured vertical offsets. We use the LaDiCaoz matlab tool (Haddon et al., 2016) which uses the lidar digital elevation model and the mapped fault trace and riser edges to calculate both vertical and lateral offset of the terrace. After the tool calculates the optimal offset it creates a back slipped lidar hillshade that we visually asses for the quality of the slip reconstruction. Lateral offset of the T_1 terrace riser calculated by the LaDiCaoz

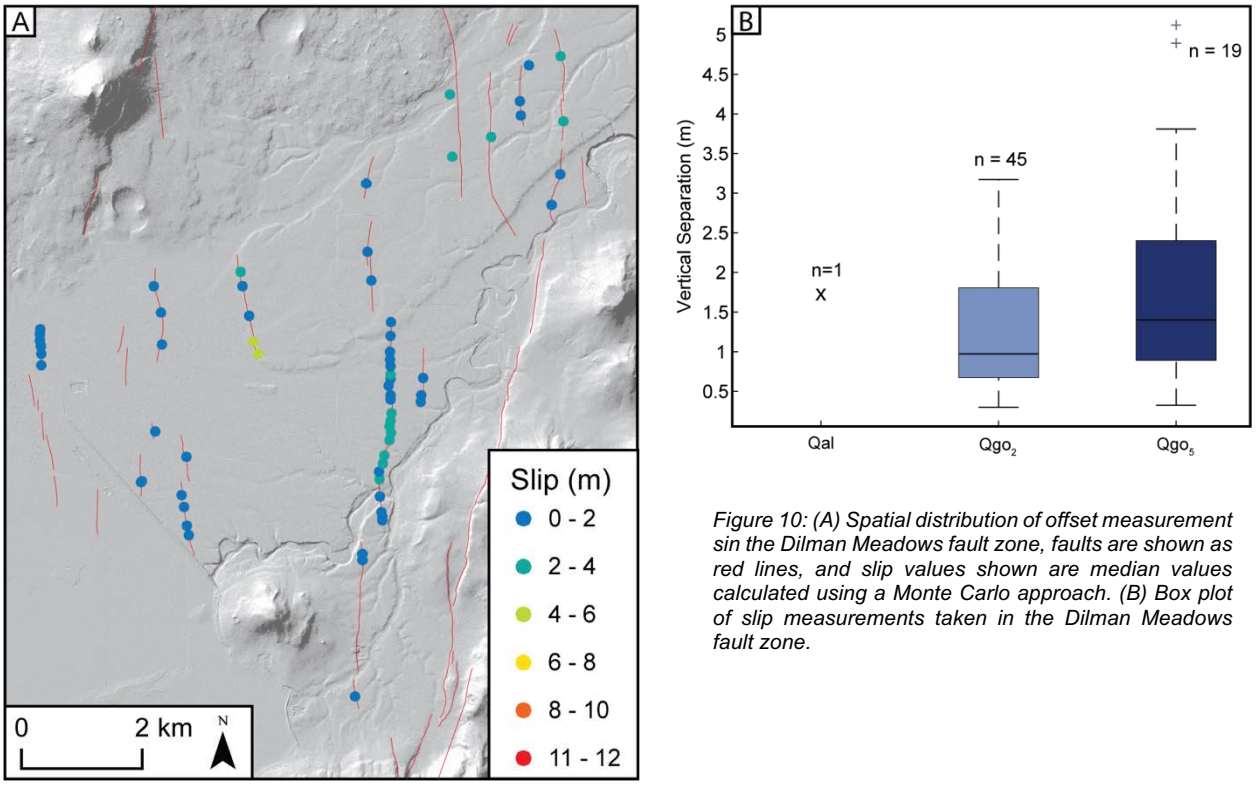

Figure 10: (A) Spatial distribution of offset measurement sin the Dilman Meadows fault zone, faults are shown as red lines, and slip values shown are median values calculated using a Monte Carlo approach. (B) Box plot of slip measurements taken in the Dilman Meadows fault zone.

tool is 1.5 + 0.5/-1.5 m, and the vertical offset is 1.5 ± 0.1 m. The vertical offset measured across the T_1 terrace using the Monte Carlo approach was 1.7 ± 0.1 m, which is comparable to the vertical offset measured using LaDiCaoz. Lateral and vertical offsets of the T_3 terrace are 6.5 +2/-0 m and 1.6 +0.2/0.4 m respectively, and the vertical offset measured using the Monte Carlo

approach was 1.6 ± 0.03 m. Lateral and vertical offsets of the T_4 terrace are 11.1 + 3.4/-0.2 m and 3.4 +0.4/0.1 m respectively, and vertical offset measured using the Monte Carlo approach is 3.4 ± 0.1 m. The similarity in vertical offset measurements between the two approaches is compelling however it is unclear if the lateral offset has been exaggerated in the loose tephra deposit due to erosion of the surface.

^{3}He Cosmogenic Surface Exposure Dating

Using cosmogenic exposure dating techniques allows us to determine numerical ages of glacial deposits in the central Oregon Cascades. We use boulder exposure dating methods in the White Branch fault zone on moraines thought to correlate to the last glacial maximum (LGM) corresponding to marine isotope stage 2 (MIS 2) at ~21 ± 2 ka (Mix, 2001). In the White Branch Valley region, boulders on moraines previously mapped as predating the LGM are not present or challenging to find. In the Shukash Basin, we collected samples from the two depth profiles to date outwash surfaces that appear to be older than the LGM. Outwash terraces in the Sierra Nevada of California appear to be to be more stable and recorded more reliable ages than steep moraine crests that recorded similar ages with larger uncertainties (Rood et al., 2011). We correlate ages between the White Branch Valley and the Shukash basin by measuring an outwash terrace in the Shukash Basin that is LGM equivalent to determine if ice was present at both locations during the LGM. By linking LGM chronologies across the High Cascade crest, our exposure ages on the older outwash surfaces on the east side indicate that there are time equivalent pre-LGM moraines on the west side of the Cascades in the White Branch Valley area.

We sampled boulders that met the following criteria: 1) the size of a boulder should be >1 m in diameter, 2) the location should be within 2 m of the crest of the moraine, 3) degree of

exhumation must be low, as evidenced by a similar degree of weathering on all sides, 4) degree of weathering must be low, as evidenced by the presence of intact weathering rinds showing the original outer edge of the boulder, and 5) ideally a minimum of four boulders would be sampled for an average age (Putkonen and Swanson, 2003). In the White Branch fault zone boulders in the older moraines (Qg_5, Qg_6) did not meet these criteria, and we were only able to date three last glacial maximum moraines in the Qg_2 moraine complex.

Depth profiles are used to date outwash surfaces, where a single depositional event can be sampled at fixed depth intervals. Depth profiles can show an exponential decrease in the cosmogenic ^{3}He production as long as there is no post deposition mixing of the material, and erosion rates of the surface are low (Rood et al., 2011). We collected at least six samples at 15 cm intervals beginning at the top of the outwash surface, except in the case of DM_DP_01 where root stirring had potentially occurred, and the loose nature of the Mazama tephra made it impossible to collect the outwash deposit without also mixing in the Mazama tephra. At each sampling horizon, we used a trowel to expose fresh, undisturbed material, being careful not to incorporate material from above. We were able to collect samples from both of the larger outwash surfaces in the Shukash basin (Supplementary S4).

Boulder dating in the White Branch fault zone

Assessing the ages of surfaces and landforms using exposure dating methods relies on nuclide production in minerals as a result of cosmic ray bombardment (Ivy-Ochs and Kober, 2008). As secondary cosmic rays bombard the surface they cause spallation reactions in minerals up to depths of about 3-m below the surface; these reactions result in the production of cosmogenic nuclides (Darvill, 2013). Common target nuclides in tectonic geomorphology are ^{10}Be and ^{26}Al, which are produced on quartz. Given the dominance of basalt and basaltic

andesite in the Oregon Cascades we targeted ^{3}He, produced in pyroxene and olivine phenocrysts in intermediate volcanic rocks (Gosse and Phillips, 2001). Recent studies (Speth et al., 2018) highlight the utility of this technique in central Oregon. The ^{3}He concentration in a moraine boulder reflects a combination of inheritance or non-cosmogenic concentrations of ^{3}He, length of time the boulder has been exposed to cosmic rays at the surface, shielding (from snow, soil, forest cover), and erosion. Inherited concentrations of ^{3}He in a moraine boulder represent prior exposure to cosmic rays, and non-cosmogenic pathways of ^{3}He production within the boulder such as the neutron capture on ^{6}Li, which can account for ~1.5 – 6 % of cosmogenic ^{3}He concentration in a basalt rock (Dunai et al., 2007). Inherited concentrations lead to biasing towards older model ages. Erosion, including erosion of the boulder surface and erosion of the landform, leading to exhumation or diffusion, lowers the observed concentration of ^{3}He therefore biasing to younger ages (Ivy-Ochs and Kober, 2008; Amidon and Farley, 2011).

We collected and analyzed 22 boulder samples from Qg_2, and one shielded sample from a quarry dug in the Basalt of Two Butte (Qbtb) (Figure 3a). There were few boulders >1 m in the area resulting in minimal sampling opportunities along the moraine crests leaving us to sample several boulders that were <1 m in diameter. We used a hammer and chisel to remove ~ 2.5 kg of the outer few centimeters of intact weathering rind form the tops of the boulders (Supplementary S14-16). On average, snow covers this region for four months of the year, but because of the dense forest cover we are unable to estimate the thickness of the annual winter snow cover, and thereby the effect of snow shielding. We do not apply a snow correction because of a lack of constraints, and as a result, our ages may underestimate the actual ages by some amount (Licciardi et al., 2004).

Pyroxene and olivine grains were isolated during mineral separation at Middlebury College, Vermont by crushing and sieving samples to 425µm - 125µm, then by using standard heavy liquid and magnetic separation techniques. We crushed ~ 450 mg of the mineral separate per sample at Western Washington University to ~10 – 50 µm under ethanol to release trapped magmatic gas and other inclusions, ethanol and remaining powder were drained from the samples. Nobel gas mass spectrometry was used to measure the ^{3}He concentrations in the samples at the Berkeley Geochronology Center. We encapsulated ~140 mg aliquots in Ta packets and heated the packets under vacuum using a 150W diode laser with coaxial optical pyrometer, allowing feedback control of the laser to achieve a prescribed pyrometer temperature. The samples were kept at 1200ºC for 15 minutes to release all of the He, gasses released were then reacted with SEAS (Societá Apparecchi Elettrici e Scientifici, Electrical and scientific components company) getters and frozen to activated charcoal at 11.5 K and warmed to 33 K at which point He was released into the mass spectrometer. The abundances of He were quantified by comparing peak heights from aliquots of custom-mixed He gas standards. Baratron capacitance manometers were used to calibrate the ^{3}He and ^{4}He concentrations in the standards. The total uncertainties reported for the He concentrations include uncertainties from blank subtraction, counting statistics, and reproducibility of gas standard analyses. Analysis of the CRONUS-P pyroxene standard (Blard et al., 2015) on this system during the period of these measurements yielded $8.24 \pm 4.00 \times 10^{6}$ atoms g^{-1} ^{3}He and 1.77 ± 4.36 ^{4}He (mean and standard deviation of 25 measurements).

We calculate exposure ages using version 3 of the online CRONUS-Earth calculator (Balco et al., 2008) (https://hess.ess.washington.edu/math/v3/v3_age_in.html). The ^{3}He concentration found in the shielded sample is an order of magnitude lower than the boulder samples which was

expected, because basalt has low U/Th and low Li concentrations which are the drivers of nucleogenic production of ^{3}He; subtracting the shielded concentrations from the total ^{3}He concentrations in each boulder had little effect (Amidon and Farley, 2011). To use the age calculator requires an erosion rate be known independently for each boulder, but due to variability in texture and vesicularity of the source rock, actual erosion rates are most likely variable depending on where in the lava flow each boulder originated. Boulders that originated in a more vesicular section of the flow might have higher erosion rates than a boulder originating from a less vesicular section of the flow. In the absence of independently known specific erosion rates values for each boulder, we applied three different erosion rate scenarios to the age calculations: 1) no boulder erosion, 2) an erosion rate of 1 mm/kyr, and 3) a maximum plausible erosion rate of 3 mm/kyr (Speth et al., 2018). We report exposure ages calculated using the 1 mm/kyr scenario based on weathering rind thickness observed in the field (Table 1).

The age results of the boulder samples are displayed using normalized kernel density plots (Figure 11). The plots use Gaussian distributions to show individual ages and uncertainties for each sample based on the 1 mm/ kyr erosion rate scenario, which are calculated using Gaussian distribution methods described in Zechar and Frankel (2009) with 2σ uncertainties. The ages that do not contribute to the highest peak in the cumulative probability function are excluded from the preferred calculated ages reported (Speth et al., 2018). A reduced χ^2 statistic computed shows that uncertainty within the measurements is likely due to scatter in the data and not geomorphic processes that would tend to artificially lower the apparent age of the unit (Table 2).

TABLE 1. SUMMARY OF ^{3}He MEASUREMENTS AT THE WHITE BRANCH FAULT ZONE, OREGON, USA

Sample name	Unit	Latitude (DD)	Longitude (DD)	Elevation (m)	Thickness (cm)	Shielding factor	Measured [^{3}He] (10^{6} atoms g^{-1})	Corrected [^{3}He] (10^{6} atoms g^{-1})	Measured [^{4}He] (10^{11} atoms g^{-1})	Minimum exposure age (ka)[a] erosion rate: 0 m/m.y.	Maximum exposure age (ka)[b] erosion rate: 3 m/m.y.	Preferred exposure age (ka)[c] erosion rate: 1 m/m.y.
Shielded samples												
WB18-S01	Qbtb	44.4142	-122.0083	1442	3	1	0.30 ± 2.60	—	0.838 ± 3.15	—	—	—
Qg_{2b} terminal moraine												
WB18-01	Qg_{2b}	44.1937	-122.9452	1281	3	0.999	6.64 ± 0.40	6.34 ± 0.40	2.75 ± 0.24	19.3 ± 2.6	20.3 ± 2.8	19.6 ± 2.7
WB18-02	Qg_{2b}	44.1941	-121.9452	1284	3	0.999	7.61 ± 0.36	7.31 ± 0.36	18.9 ± 4.29	22.2 ± 2.8	23.6 ± 3.2	22.7 ± 2.9
WB18-03	Qg_{2b}	44.1916	-121.9370	1351	3.5	0.999	7.02 ± 0.38	6.72 ± 0.38	1.76 ± 0.14	19.5 ± 1.8	20.6 ± 2.0	19.8 ± 1.8
WB18-04	Qg_{2b}	44.1918	-121.9384	1349	3.5	0.999	7.25 ± 0.41	6.95 ± 0.41	0.35 ± 0.13	20.2 ± 2.6	21.3 ± 2.9	20.5 ± 2.7
WB18-05	Qg_{2b}	44.1954	-121.9488	1254	3.5	0.999	11.2 ± 0.53	10.9 ± 0.53	0.65 ± 0.15	33.4 ± 3.0	37.5 ± 3.6	35.1 ± 3.1
WB18-06	Qg_{2b}	44.1965	-121.9501	1256	2.5	0.999	16.4 ± 0.76	16.0 ± 0.76	1.91 ± 0.18	49.8 ± 6.0	57.7 ± 8.1	52.1 ± 6.6
WB18-07	Qg_{2b}	44.1974	-121.9511	1249	3	1.00	6.41 ± 0.37	6.11 ± 0.37	2.82 ± 0.12	19.1 ± 2.5	20.1 ± 2.8	19.4 ± 2.6
WB18-08	Qg_{2b}	44.2003	-121.9508	1246	3.5	0.999	6.61 ± 0.41	6.31 ± 0.41	1.52 ± 0.18	19.8 ± 2.7	20.9 ± 3.0	20.2 ± 2.8
WB18-09	Qg_{2b}	44.1992	-121.9517	1241	3	0.999	2.36 ± 0.24	2.06 ± 0.24	2.65 ± 0.11	6.5 ± 1.3	6.6 ± 1.4	6.5 ± 1.3
WB18-16	Qg_{2b}	44.1923	-121.9416	1305	3	0.999	5.02 ± 0.35	4.72 ± 0.35	38.4 ± 0.86	14.1 ± 2.0	14.7 ± 2.2	14.3 ± 2.1
Qg_{2c} terminal moraine												
WB18-17	Qg_{2c}	44.1914	-121.9476	1263	3	0.999	8.49 ± 0.50	8.19 ± 0.50	35.2 ± 3.13	25.3 ± 3.2	27.2 ± 3.8	25.9 ± 3.4
WB18-18	Qg_{2c}	44.1922	-121.9494	1260	2	0.999	6.84 ± 0.36	6.54 ± 0.36	1.30 ± 0.16	20.1 ± 2.6	21.2 ± 2.9	20.4 ± 2.7
WB18-19	Qg_{2c}	44.1955	-121.9532	1242	2.5	0.999	5.51 ± 0.37	5.21 ± 0.37	2.48 ± 0.19	16.3 ± 1.6	17.0 ± 1.8	16.5 ± 1.7
WB18-20	Qg_{2c}	44.1996	-121.9548	1223	3.5	0.999	7.32 ± 0.37	7.02 ± 0.36	6.29 ± 0.17	22.5 ± 2.9	23.9 ± 3.2	22.9 ± 3.0
WB18-21	Qg_{2c}	44.2014	-121.9538	1231	2.5	0.999	5.32 ± 0.35	5.02 ± 0.35	1.48 ± 0.12	15.8 ± 2.2	16.5 ± 2.4	16.1 ± 2.3
WB18-22	Qg_{2c}	44.2018	-121.9506	1262	2.5	0.999	6.65 ± 0.40	6.35 ± 0.40	2.86 ± 0.14	19.5 ± 2.6	20.6 ± 2.9	19.9 ± 2.7
WB18-23	Qg_{2c}	44.2004	-121.9552	1230	3	0.999	5.91 ± 0.33	5.61 ± 0.33	0.43 ± 0.12	17.8 ± 2.3	18.7 ± 2.6	18.1 ± 2.4
Qg_{2d} lateral moraine												
WB18-10	Qg_{2d}	44.2439	-121.9821	1162	2	1.000	6.38 ± 0.41	6.08 ± 0.41	0.56 ± 0.13	20.1 ± 1.9	21.2 ± 2.2	20.7 ± 2.0
WB18-11	Qg_{2d}	44.2437	-121.9837	1139	2.5	0.999	6.41 ± 0.36	6.11 ± 0.36	2.76 ± 0.12	20.6 ± 2.7	21.9 ± 3.1	21.1 ± 2.8
WB18-12	Qg_{2d}	44.2438	-121.9849	1146	3	1.000	6.72 ± 0.42	6.42 ± 0.42	310 ± 6.92	21.7 ± 2.1	23.1 ± 2.3	22.1 ± 2.1
WB18-14	Qg_{2d}	44.2426	-121.9938	1076	3	1.000	10.2 ± 0.50	9.88 ± 0.50	0.411 ± 0.17	35.3 ± 3.1	39.1 ± 3.8	36.5 ± 3.3
WB18-15	Qg_{2d}	44.2426	-121.9957	1079	3	0.999	11.6 ± 0.47	11.27 ± 0.47	8.56 ± 0.38	40.1 ± 3.4	45.2 ± 4.4	41.6 ± 3.7

[a-c] Exposure ages calculated using the CRONOUS-Earth exposure age calculator (Balco et al., 2008) assuming a minimum erosion rate of) M/Myr, a maximum erosion rate of 3 M/Myr (Cerling et al., 1990), and a preferred erosion rate of 1 M/Myr based in observation of the sample d boulders (Speth et al., 2019). Red values are excluded from the average age reported.

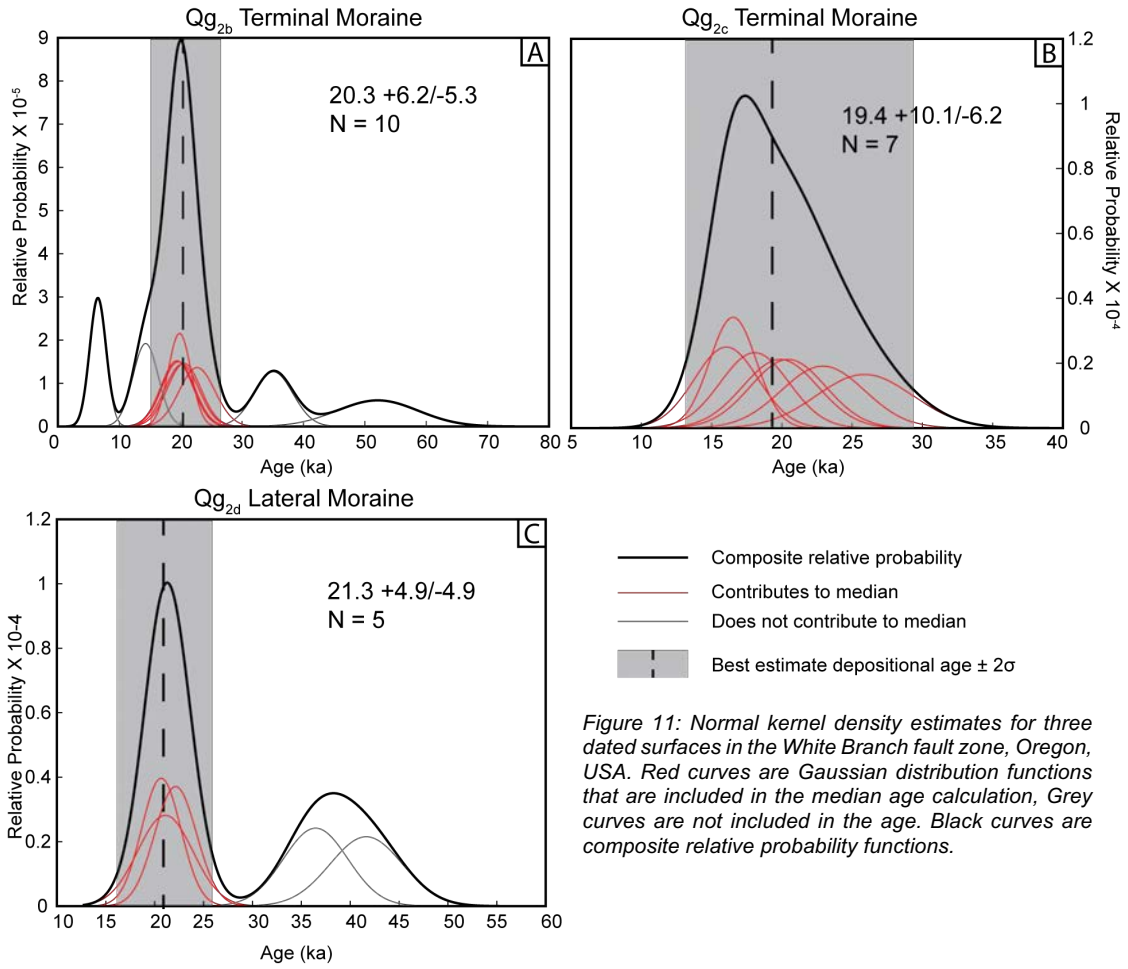

Figure 11: Normal kernel density estimates for three dated surfaces in the White Branch fault zone, Oregon, USA. Red curves are Gaussian distribution functions that are included in the median age calculation, Grey curves are not included in the age. Black curves are composite relative probability functions.

TABLE 2. SURFACE AGE SUMMARY

Mean Age (kyr)	n	Reduced χ^2 [a]	p [b]	Oldest Age (kyr)	Best estimate depositional age (kyr)
Qg_{2b} Terminal Moraine					
20.3 +6.2 /-5.3	5	0.24	1	22.7 ± 2.9	20.3 +6.2 /-5.3[c]
Qg_{2c} Terminal Moraine					
19.4 +10.1/-6.2	7	1.92	0.93	25.9 ± 3.4	19.4 +10.1/-6.2[c]
Qg_{2d} Lateral Moraine					
21.3 ± 4.9	3	0.13	0.94	22.1 ± 2.1	21.3 ± 4.9[c]

[a] A statistical measure of the scatter of ages from surface
[b] The probability that scatter is from measurement uncertainty alone. A value <0.05 indicates that some geomorphic processes (e.g. exhumation, inheritance) may be responsible for some of the scatter
[c] Calculated after the removal of outliers

The youngest dated landform is a terminal moraine in Qg_{2c}; the ages used for this calculation show the most scatter of the three dated surfaces. We collected seven samples from the Qg_{2c}

moraine that do not show any cluster of ages but a relatively even distribution that ranges from 16.1 ± 2.3 ka to 25.9 ± 3.4 ka; and for this reason we included all seven ages in the reported age of 19.4 +10.1/-6.2 ka (Figure 3c). We sampled 10 boulders from a terminal moraine in unit Qg_{2b}, which must be younger than the terminal moraine in unit Qg_{2c} due to superposition laws. The ages of the boulders range from 19.4 ± 2.6 ka to 22.7 ± 2.9 ka, not including outliers. The age reported for the Qg_{2b} moraine excludes four outlier ages from samples WB18-05 (35.1 ± 3.1 ka), WB18-06 (52.1 ± 6.6 ka), WB18-09 (6.5 ± 1.3 ka), and WB18-16 (14.3 ± 2.1 ka), we chose to exclude these ages as they do not contribute to the largest peak in the summed probability density function. We report an age of 20.3 +6.2/-5.3 ka for the Qg_{2b} moraine (Figure 3c). The oldest dated landform is a lateral moraine in Qg_{2d}, where we excluded two of the five ages from samples we collected, WB18-14 (36.5 ± 3.3 ka) and WB18-15 (41.6 ± 3.7 ka), because the ages did not contribute to the largest peak in the summed probability density function. The ages used for the reported age of the Qg_{2d} moraine range from 20.7 ± 2.0 ka to 22.1 ± 2.1 ka, and the age we report for this moraine is 21.3 ± 4.9 ka (Figure 3d).

Depth profiles from the La Pine Graben

^{3}He cosmogenic nuclide dating methods can also be applied to estimate the resident time of an outwash deposit at the surface. As material is deposited at the surface it is bombarded with secondary cosmic rays, much like a boulder sitting on the surface of a moraine. Unlike a moraine boulder however, the exponential decrease in production rate, P , of cosmogenic nuclides with depth, z , must be addressed when dating deposits (Anderson et al., 1996). In addition to changes in production rate, samples collected for a cosmogenic depth profile are likely to have cosmogenic inheritance, N_{inh}, that can be estimated by collecting several samples at multiple

depth intervals below the surface (Gold et al., 2013). Inheritance found in in depositional units can be from several sources: 1) N_{pre}, exposure during previous transport and deposition cycles, 2) N_{exh}, exposure during exhumation, 3) N_{trans}, exposure during transport, and 4) N_{dep}, exposure during deposition, all sources are then combined for a total inheritance value N (Anderson et al., 1996).

$$N_{inh} = N_{pre} + N_{exh} + N_{trans} + N_{dep} = N_{in} + N_{dep} \quad (1)$$

We cannot directly measure the source of inherited cosmogenic nuclides, but we can model it using the cosmogenic radio nuclide (CRN) concentrations at multiple depths within the unit. Post-depositional erosion of the surface will tend to produce artificially younger ages and must be addressed when calculating the age of a deposit. In the La Pine graben however, the amount of surface erosion cannot be directly measured and is assumed to be stable since the 2 m thick blanket of volcanic tephra that was deposited 7682 – 7584 cal yr. B.P during the eruption of Mt. Mazama (Egan et al., 2015). The Mazama tephra layer not only obscures the amount of erosion that has occurred on the underlying units, but also reduces the production of CRNs in the underlying units since tephra deposition. The relationship between CRN concentration and depth can be calculated using the following equation:

$$N(z) = N_o e^{-z/\Lambda} + N_{inh} \quad (2)$$

Where $N(z)$ is the concentration of CRNs at depth z, N_o is the concentration at the surface, Λ is the attenuation length for production by high energy spallation (largely a function of material density), and N_{inh} is the inherited component of CRNs (Speth et al., 2018).

In the Dilman Meadows fault zone we target two glacial outwash surfaces: 1) Qgo_5, the highest terrace surface in in the mapping area, and 2) Qgo_2, a separate terrace deposit inset into Qgo_5. As with the moraine boulders from White Branch Valley, we targeted pyroxene and

olivine minerals in the clasts because of the abundance of basalt and basaltic andesite. We dug two ~2.5 m deep pits into the outwash surfaces and collected ~2.5 kg of material at each 15 cm interval. The samples were prepared using the same methods as those for the boulder samples at Middlebury College, Vermont, and at Western Washington University. We analyzed the samples at the Berkeley Geochronology center using the same methods as those for the boulder samples. We fit equation 2 to the data using a Monte Carlo simulation that samples from a random distribution of erosion rates ranging from 1 mm/kyr to 15 mm/kyr for both Qgo_5 and Qgo_2 over 10,000 times. As erosion of the deposit occurs, the material with the highest concentrations of ^3He is removed, artificially lowering the apparent age of the deposit. Based on production rates and the concentration of ^3He in the Qgo_5 deposit, however, we know that for the older deposit to have accumulated the amount of ^3He recorded the surface erosion rate must be lower than 15 mm/yr. This erosion rate can be used for the age calculation of the younger deposit because the surface erosion rate of the younger deposit must be the same as limited rate based on the concentration of ^3He found in the older Qgo_5 deposit. We assume the surface erosion rate has been constant and use 15 mm/yr as the erosion rate for both age calculations.

The equation is fit by minimizing the sum of the squares of the differences between the measured ^3He concentrations and the values predicted by the function. The best fit was then solved for the surface concentration, which was then used to calculate the corresponding surface age using 150 g/cm^3 for λ (Gosse and Phillips, 2001), and an tephra density of 0.74 g/cm^3 (Supplementary S17), and density range for the sampled material of 1.25 -2.5 g/cm^3 (common density for basalt and basaltic andesite). The age of the Mazama tephra deposition, which reduces the production of ^3He in the outwash at ~7.6 ka, was added to the ages calculated for both outwash surfaces.

The depth profile pit for the older glacial outwash surface (Qgo_5) was dug in the side of an abandoned quarry (Figure 6a). From the Qgo_5 pit we collected seven samples at 15-cm intervals beginning 30 cm below the top of the outwash unit (Figure 12a). The loose structure of the Mazama tephra above the outwash unit made sampling the surface of the outwash impossible

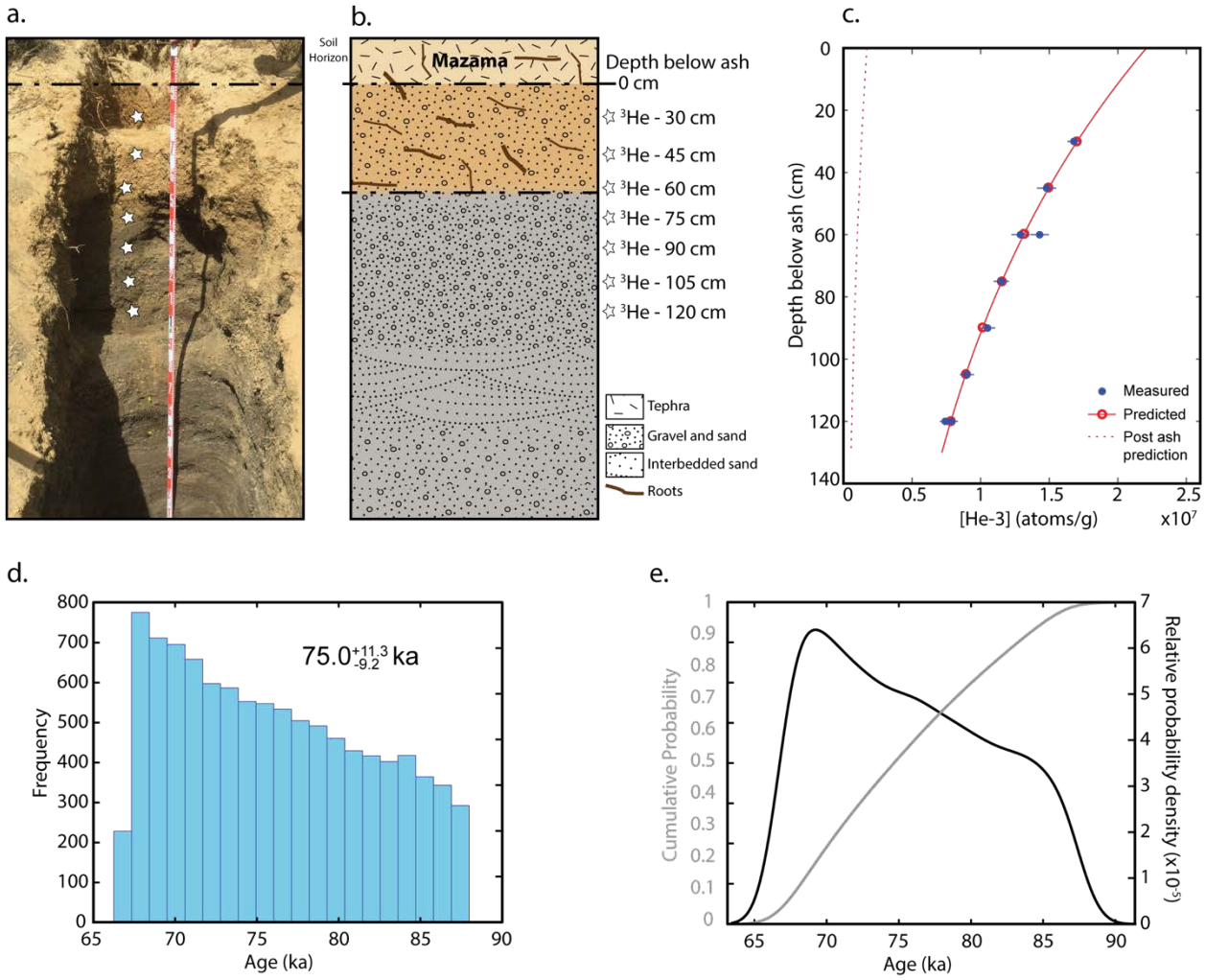

Figure 12: (A) Photograph of DM_DP_01 pit looking west. White Stars are ^{3}He CRN gravel and sand locations. Black dashed line represents the base of the Mazama ash deposit. Color change below ash indicated oxidation of clasts in deposit. (B) Stratigraphic column showing the homogeneity of the deposit below the ash. (C) ^{3}He cosmogenic depth profile using a 10 mm/kyr erosion rate, blue dots are measured concentrations and errors are 2σ about the mean. The red curve is the best fit prediction, found by minimizing the chi-squared statistic. (D) Age distribution predicted from 10,000 scenarios of the Monte Carlo simulation where erosion rates range from 1 mm/kyr to 10 mm/kyr. Age reported is the median of the distribution with 2σ errors about the median € Black curve is the relative probability density and grey curve is the cumulative probability function for erosion rates ranging from 1 mm/kyr to 10 mm/kyr.

without mixing large amounts of tephra in with the outwash gravels, and several large roots in the upper 30-cm of the outwash surface made sampling at those depths not ideal due to the potential for root mixing of the deposit effecting the concentration of CRNs measured (Figure

12b). The surface of the outwash has significant soil development to depths of 60 cm and weathering of individual grains is apparent implying that the surface has not been stripped. The grains collected had high percentages of olivine relative to pyroxene. The best fit equation for the Qgo_5 samples shows no inherited concentrations of ^3He (Figure 12c) and using the Monte Carlo simulation we report an age of 75.0 +11.3/-9.2 kyr (Figure 12d). Cumulative probability and Relative probability graphs show that in a range of ages for Qgo_5 a younger age is preferred (Figure 12e).

The depth profile pit for the younger glacial outwash surface (Qgo_2) was dug into the upthrown block east of a fault scarp in the center of unit Qgo_2 (Figure 6a) this location was chosen based on permits for digging. From the Qgo_2 pit we collected six samples at 15 cm intervals beginning at the top of the outwash unit; the tephra at this location had more structure and we were able to collect samples without mixing materials (Figure 13a). Small roots occur throughout the deposit but did not appear to have significantly mixed materials (Figure 13b). Like the surface of the Qgo_5 deposit there were few signs of surface weathering, but the grains in Qgo_2 contained higher percentages of pyroxene compared to olivine. There was a minor amount of inherited ^3He in the sample when the best fit equation was calculated for the unit; there was an exponential decrease in the concentration of ^3He, indicating that the outwash was deposited rapidly (Figure 13c). We report an age of 20.0 + 0.04/-0.03 kyr from the Monte Carlo simulation (Figure 13d) and show that the age distribution is uniform in the cumulative probability and relative probability density graphs (Figure 13e).

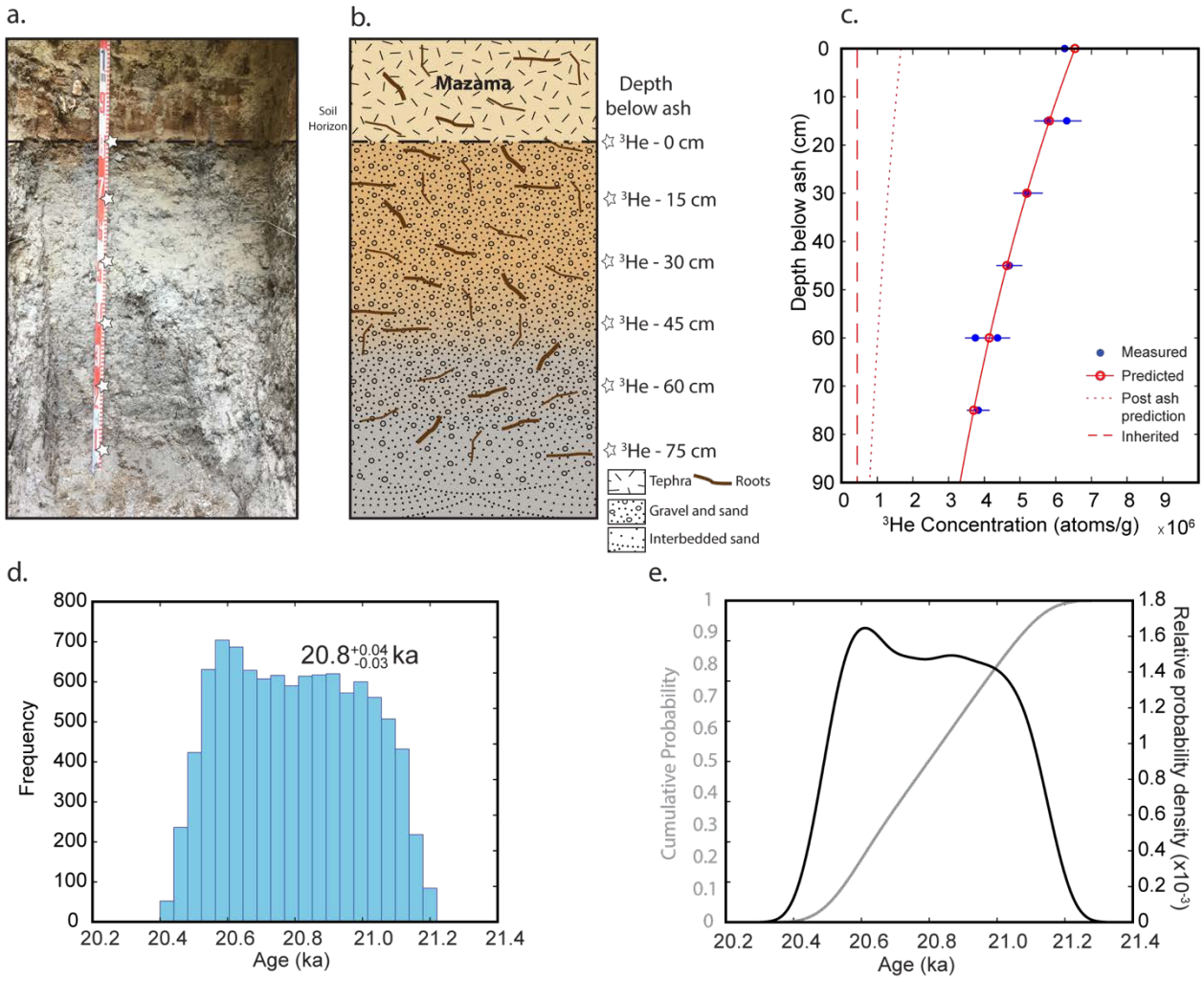

Figure 13: (A) Photograph of DM_DP_02 pit looking west. White Stars are ^{3}He CRN gravel and sand locations. Black dashed line represents the base of the Mazama ash deposit. (B) Stratigraphic column showing the homogeneity of the deposit below the ash. Color change below ash indicated oxidation of clasts in deposit. (C) ^{3}He cosmogenic depth profile using a 10 mm/kyr erosion rate, blue dots are measured concentrations and errors are 2σ about the mean. The red curve is the best fit prediction, found by minimizing the chi-squared statistic. (D) Age distribution predicted from 10,000 scenarios of the Monte Carlo simulation where erosion rates range from 1 mm/kyr to 10 mm/kyr. Age reported is the median of the distribution with 2σ errors about the median € Black curve is the relative probability density and grey curve is the cumulative probability function for erosion rates ranging from 1 mm/kyr to 10 mm/kyr.

Discussion

Glacial Chronology of the Central Oregon Cascades

^{3}He cosmogenic surface exposure dating allow us to further develop an emerging glacial chronology of the Central Oregon Cascades. In the White Branch fault zone, on the west side of the Cascades, boulders are rarely if ever preserved on moraines older than the LGM (owing to high erosion rates, high soil production, logging disturbance, etc.). As a result, we are only able

to directly date two terminal moraines and one lateral moraine in the youngest glacial deposits (Qg_2). These ages overlap within uncertainty at ~20 kyr for all three moraines (Figure 3a, 12). The ages of the moraines confirm that the White Branch fault zone was glaciated during the last glacial maximum (MIS 2: ~21 ± 2 ka) (Mix, 2001), locally recognized as the Suttle Lake advance of the Cabot Creek glaciation (Scott, 1977). Suttle Lake deposits were previously identified in the White Branch fault zone, but ages were based on moraine preservation, soil development, and a thickness of weathering rinds on clasts in soils formed in the deposits, as well as correlation to Scott's (1977) mapping (Sherrod et al., 2004). Moraines correlated to Suttle Lake deposits north-east of the Twin Lake Maars could have contributed sediment to the Shukash Basin during the LGM. Our exposure age of 20.8 +0.04/-0.03 kyr for the younger Qgo_2 outwash surface in the basin supports this inference and connects the timing of the last glacial maximum in the Shukash Basin across the Cascade crest to the ~20 kyr moraines in the White Branch Valley. Our LGM ages also connect these moraines to ^{10}Be dated moraines in the Wallowa Mountains in eastern Oregon (17.0 ± 0.3 kyr and 21.1± 0.4 kyr) (Licciardi et al., 2004), and to ^{3}He exposure ages in the Klamath Basin in southern Oregon of moraines (17.6 ± 2.1 kyr) and an outwash age (20.4 ± 5.3 kyr) (Speth et al., 2018); the latter in particular, matches our outwash age almost exactly. Similarly, the timing of the LGM in Oregon overlaps with Leavenworth I at 16.1 ± 1.1 ka and Leavenworth II at 19.1 ± 3.0 ka glacial sequence in the eastern Cascades in Washington (Porter and Swanson, 2008). Multiple glacial landforms dated in eastern California's Sierra Nevada reveal a similar last glacial maximum Tioga age of 18.8 ± 1.0 ka (e.g., Rood et al., 2011).

Scott (1977) recognized older Late Pleistocene glacial deposits on the eastern flanks of Mt. Jefferson and Three fingered Jack (Figure 2), related to what he termed the Jack Creek

glaciation, but was unable to determine if the deposit was related to episodes of glacier expansion at 40-80 ka or 120-200 ka (e.g., MIS 3/4 or 6) (Figure 2). Speth et al. (2018) identify a cluster of ^{3}He exposure ages of boulders on moraines dating to 97.6 ± 12.7 kyr which they correlate to the Jack Creek moraines of Scott (1977). This mean age is within error of the 75.0 +11.3/-9.2 kyr age we report for the older outwash surface (Qgo_5) in the Shukash Basin. These ages along with reported ^{36}Cl exposure ages of 71.9 ± 1.5 kyr and 92.1 ± 2.6 kyr for moraines near Leavenworth, Washington also support a MIS 5b glaciation interpreted by Porter and Swanson (2008) and by Scott (1977) for a younger possible age for the Jack Creek glaciation.

Our new mapping and ^{3}He age constraints, combined with the results of other studies mentioned above, indicate that ice extent during the penultimate glaciation was similar to, and generally slightly greater than, the LGM throughout the Cascades. On the west side of the Cascade arc in the White Branch fault zone we were unable to directly date pre-LGM glacial deposits; however the presence of the older (Qgo_5) 75.0 +11.3/-9.2 kyr outwash surface in the Shukash basin east of the crest, which we correlate to the Qg_5 glacial deposits, strongly supports the inference that ice was similarly extensive west of the Cascade crest. The preservation and appearance of the pre-LGM moraines in the White Branch Valley are similar to moraines in the intermediate deposits in the Klamath Basin, providing further evidence that the Qg_5 deposit in the White Branch Valley is likely from a MIS 5b glacial advance.

Deposits from glaciations older than MIS 5b are not apparently persevered in the Shukash basin, but moraines thought to be MIS 6 equivalent are found in the Klamath Basin (Hawkins et al., 1989). MIS 6 is dated at 144 ± 14 ka and is referred to as the Tahoe Glaciation in the Sierra Nevada (Rood et al., 2011) and in the Klamath basin a moraine boulder age of 168.9 ± 22.3 kyr was tentatively linked to MIS 6 (Speth et al., 2018). It is possible that the oldest Qg_6 glacial

deposit in the White Branch Valley is from a MIS 6 glaciation, but we do not have exposure age data to confirm this correlation. There is morphological evidence however that the Qg_6 deposit is much older than the Qg_5 and Qg_2. Moraine crests are not preserved on the Qg_6 surface and the direction of ice flow was different than during younger glaciations, evidenced by north south glacial lineations preserved on the surface of Qg_6 that are unlike the east west glacial lineations observed in the younger deposits (Supplementary S1).

In summary, we recognize three glacial advances in the central Oregon Cascades, during which synchronized smaller glaciers on the flanks of the Cascade volcanoes as well as a larger valley glacier were present on the west side of the crest in the White Branch Valley. The glaciers present in the White Branch Valley correlated to glaciers feeding outwash to the east side of the crest in the Shukash Basin.

Slip rates

We calculate slip rates from offset piercing lines such as moraine crests and terrace risers that have been offset by faulting. We then compare these to the horizontal GPS-velocity field to determine if long-term surface faulting is capable of accommodating clockwise rotation of the Siletzia domain relative to North America (McCaffrey et al., 2013; Brocher et al., 2017; Mark-Moser, 2018). The ages of glacial deposits from the LGM, MIS 5, and slip measurements calculated from the Mote Carlo simulation described previously are used to calculate slip rates for both the White Branch fault zone and the Dilman Meadows fault zone.

White Branch Fault Zone

As discussed previously, offset measurements in the White Branch Valley exhibit no correlation between age and the amount of offset measured (Figure 8). Dip slip measurements in

the White Branch fault zone range from 0.3 ± 0.1 – 12.7 ± 0.6 m; this variability comes from three, independently dated, geomorphically distinct Qg_2 moraine loops. The individual offset measurements, as well as the summed offsets from the Qg_5 moraines in the White Branch Valley show the same magnitude of offset as the independently dated Qg_2 moraines. This lack of correlation combined with highly segmented fault strands suggests that calculating temporal variability of slip rates for this zone is not feasible. Instead, we suggest that the lack of correlation between offset and surface age results from deformation being entirely post LGM. To further understand the post LGM deformation, we sum the offset across the fault zone in 1 km windows along a north south transect (Figure 15a). Along this transect, we measure between dip slip, extension, vertical separation, and the absolute values of vertical separation, to compare how the magnitude of offset varies from north to south (Figure 15a). The trend in each component of offset shows an increase near the center of the fault zone, and a general net displacement down to the west. We use the window with the largest summed slip (41.2 ± 1.8 m) for a maximum summed dip slip rate of 2.1 ± 0.1 mm/yr and a maximum summed extension rate of 1.7 ± 0.1 mm/yr since the LGM. If we consider deformation of the Qg_5 moraine complex for the White Branch Valley using our age from Shukash Basin (75.0 +11.3/-9.2 ka) the summed slip rate is reduced to 0.6 ± 0.1 mm/yr although again, we consider the overlap for individual scarp offset measurements in Qg_2 vs Qg_5 as strong evidence that all scarps in the White Branch Valley result from post LGM earthquake surface ruptures.

We can compare this summed rate calculated across multiple generations of glacial deposits with a transect along a single Qg_5 lateral moraine crest that is cut by multiple fault traces. This moraine was deposited by a valley glacier on the south side of the White Branch Valley and is the only single geomorphic feature that spans the width of the fault zone (Figure 5b and 14b).

The White Branch fault zone has a dominant net displacement down to the west, despite the Qg_5 moraine having a net displacement of 1.2 m down to the east; this is likely because the moraine primarily accommodates extension. This moraine transect has a larger summed dip slip offset (23.5 ± 1.2 m) than the corresponding summed dip slip offset from the fault zone window (18.5 ± 0.8 m), meaning the slip rate across the Qg_5 moraine is only slightly larger. This discrepancy between the 1 km summed slip window and the slip across the moraine crests is likely due to averaging of offset measurements along fault strands that we sum for the total slip value. The values of summed dip slip offset between the transect of a moraine with an inferred MIS 5 age and the summed fault zone window at that location are similar, providing more evidence that deformation in the White Branch fault zone is entirely post LGM.

Similar styles of distributed faulting in Searles Valley and Death Valley, California and along the Sierra El Mayor, Baja California, typically involve graben structures formed by normal faulting that sole into a master fault at depth (Axen et al., 1999; Hayman et al., 2003; Numelin et al., 2007). The graben style structures observed in the White Branch fault zone could be explained by a master fault at depth similar to the West Klamath Lake fault zone in southern Oregon, where along-strike variability on sub-parallel surface rupturing normal faults is likely controlled by a single fault (Speth et al., 2018). The change in net displacement of the White Branch fault zone along strike from down to the west to down to the east implies the complexity observed at the surface continues with depth. The proximity of the White Branch fault zone to the Three Sisters volcanic complex could also affect the rupture patterns similar to the 2019 Ridgecrest earthquake, where the ruptures terminated close to the Coso volcanic field due to high temperatures and greater pore pressure which weakened the crust and inhibited slip propagation (Chen et al., 2020).

The measured slip rates for the White Branch fault zone compare well with others in central Oregon. Across central Oregon, Pezzopane and Weldon (1993) measured several fault zones that show average slip rates of ~0.5 – 1 mm/yr, Mark-Moser (2018) presents a median slip rate for the Sisters Fault zone of ~0.5 mm/yr, and Speth et al. (2018) show that individual fault slip rates are small but for a master fault at the depth slip rate is ~0.3 mm/yr in the West Klamath Lake fault zone in southern Oregon. The White Branch fault zone is similar to the West Klamath Lake fault zone in that slip rates for individual faults are small but when summed across the White Branch fault zone the slip rate varies from 0.03 – 2.6 mm/yr. Calculating the average summed slip rate across the White Branch fault zone when using the summed 1km windows is 0.6 ± 0.5 mm/yr; this rate is in agreement with other slip rates calculated in the region.

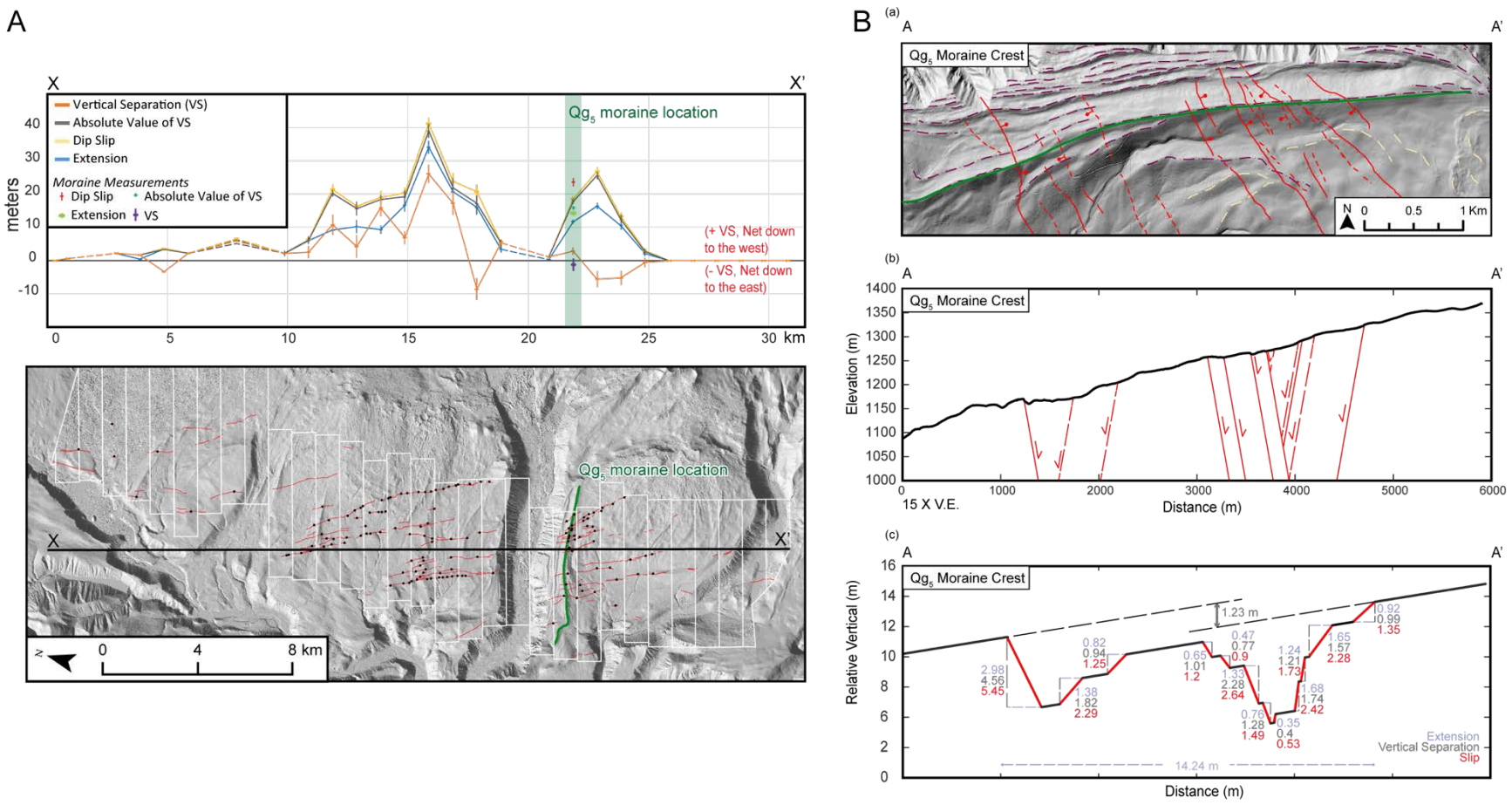

Figure 14: (A) White Branch fault zone sectioned into 1 km increments perpendicular to the strike of the fault zone. Black dots are locations of individual scarp measurements, where multiple measurements are taken on a single fault strand the slip value is averaged and used in the net slip for the km increment. Slip within each 1 km block increment is summed to show that there is more overall slip occurring in the center of the fault zone than the northern or southern extent of the fault zone. (B) Continuous moraine crest across White Branch fault zone. a) Map view of faults and moraine crests surrounding the intermediate age Qg_5 lateral moraine. b) Topographic profile to show locations of faults with interpreted projections of faults at depth. c) Conceptual diagram of moraine crest profile vertically exaggerated to show offset on individual fault scarp.

Dilman Meadows Fault Zone

Across the Dilman Meadows fault zone, offset magnitude varies as a function of surface age (Figure 10), so we consider total slip rates across multiple time intervals (Figure 15). There are post-Mazama tephra (~7.6 ka) earthquakes on the faults in the Dilman Meadows fault zone (Lyon, 2001; Vadman and Bemis, 2019) and greater offsets in the Qgo_5 than in Qgo_2, both of which represent pre-Mazama deposits. The Mazama tephra may have muted the surfaces and scarps, but it did not completely obscure them, therefore, we use the age of the outwash deposits to establish minimum summed slip rates for Qgo_5 and Qgo_2. There is one post-Mazama unit (Qal), which is offset; therefore, we use age of the Mazama tephra as a maximum age of the unit to calculate a minimum rate for that time interval (Table 3) (Lyon, 2001; Vadman and Bemis, 2019).

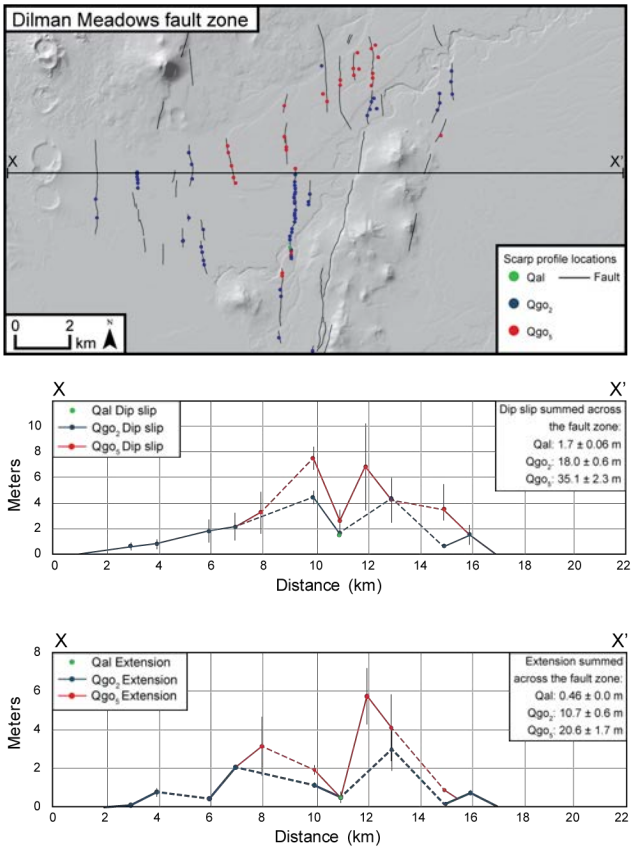

Figure 15: Top panel showing map of Dilman Meadows fault zone. Scarp Profiles are colored by geologic unit they measured in. On individual fault strands offset measurements were averaged and projected to the X-X' profile. Top graph averaged slip per fault strand per unit from west to east. Bottom graph shows averaged extension per fault strand per unit from west to east.

Previous studies on the Twin Lake Maars fault just west of the map area have shown evidence of post-Mazama tephra rupture (Vadman and Bemis, 2019), as well as along the Dilman Meadows fault located within the map area. Lyon (2001) trenched the Dilman Meadows

fault and found evidence of at least one post-Mazama tephra deposition earthquake (trench location shown in Figure 7).

TABLE 3. DILMAN MEADOWS FAULT SLIP RATES

Unit	Total slip measured	Age used for calculation	Slip Rate	Extension Rate
Qal	1.70 ± 0.06 m	7682 – 7584 ka	0.22 ± 0.02 mm/yr	0.05 ± 0.01 mm/yr
Qgo_2	18.0 ± 0.03 m	~20.8 ka	0.8 ± 0.03 mm/yr	0.4 ± 0.03 mm/yr
Qgo_5	35.1 ± 2.3 m	75 +11.3/-9.2 ka	0.5 ± 0.1 mm/yr	0.3 ± 0.02 mm/yr

** Dilman Meadows Fault Slip rates from scarp profiles measured from terraces surfaces in units Qgo_5, Qgo_2, and Qal. Profile locations are shown in Figure 7, and Offsets a measured using meadows described in the Scarp Profiles section.*

We measured offsets in a sequence of terrace surfaces that are transected by the Dilman Meadows fault and use the age of Mazama tephra deposition and our new outwash exposure ages to calculate slip rates (Figure 7). From youngest to oldest the Quaternary alluvium (Qal) is a mixture of outwash gravels and reworked Mazama tephra; therefore, it must post-date the deposition of Mazama tephra. In the Qal unit we recognize the lowest elevation terrace (T_o) as the active channel deposit and using lidar we are able to determine that the T_o terrace is not offset by the Dilman Meadows fault. Terrace tread T_1 is higher in elevation than T_o but still within the Qal unit and is offset by the Dilman Meadows fault 1.7 ± 0.1 m vertically and 2.0 ± 0.5 m laterally. On the southern side of the Deschutes River, terrace tread T_2 is cut into the Qgo_2 outwash and does not extend to the fault. Terrace tread T_3 is the surface of the Qgo_2 outwash deposit and is vertically offset north of the Deschutes River 2.0 ± 0.0 m and south of the river 1.6 ± 0.0 m and on the southern exposure we measured 6.5 ± 2.0 m of lateral offset. Terrace T_4 is the highest terrace tread offset by the Dilman Meadows fault 3.1 ± 0.1 m vertically and 11.1 ± 3.4 m laterally and is the Qgo_5 surface south of the Deschutes River. We interpret the similarities in offset values between T_1 and T_3 to mean that the terrace surfaces have experienced the same number of earthquakes since deposition of Mazama tephra and use the age of Qgo_2 to calculate

oblique slip rates of 0.1 – 0.3 mm/yr for the Dilman Meadows fault for these terraces. We infer from the larger offset measured across Qgo_5 that terrace T_4 has experienced multiple earthquakes, and in a trench north of the Deschutes River there is evidence for at least one pre-Mazama earthquake (Lyon, 2001); we use the age of the Qgo_5 deposit to calculate an oblique slip rate of ~0.2 mm/yr for this terrace.

Using offsets measured in the trench north of the Deschutes River across the Dilman Meadows fault and general ages of glaciation, Lyon (2001) reports intervals of slip rates for the Dilman Meadows fault. The slip rate reported by Lyon (2001) for the Dilman Meadows fault between 18 – 7.6 ka is 0.3 mm/yr, which is within the range of slip rates that we report for the Dilman Meadows fault of 0.1 – 0.3 mm/yr. The Dilman Meadows fault could account for nearly half of the total slip rate across the entire Dilman Meadows fault zone.

Regional Implications

Continuous clockwise rotation of crustal domains in the pacific northwest is evidenced by paleomagnetic rotations and geodesy (Wells et al., 1998; McCaffrey et al., 2007). The crustal domains are defined using seismicity patterns, GPS data, and known fault systems with the caveat that with more fault data the model can be further refined (McCaffrey et al., 2007; Savage and Wells, 2015). East of the

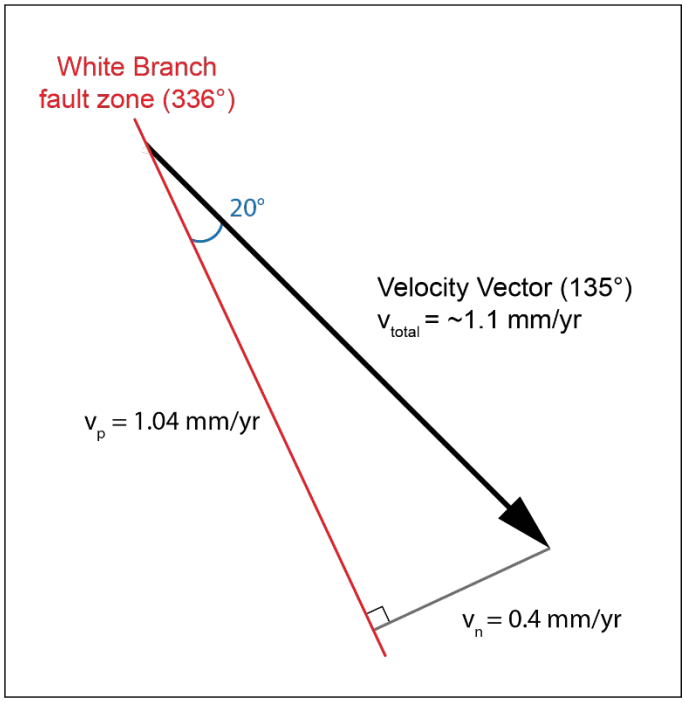

Figure 16: Deconstructed velocity vector (black line) for the southern Oregon coast ranges and eastern Oregon block boundary from McCaffrey et al., (2007). Red line represents average strike of the White Branch fault zone with the predicted velocity for fault parallel motion. The grey line represents the fault normal vector and predicted velocity of fault normal motion.

Three Sisters volcanic complex (Figure 2), McCaffrey et al. (2007) define a block boundary between the southern Oregon Coast Range domain and eastern Oregon domain. The slip vector calculated at this block boundary is ~1.1 mm/yr to the southeast, nearly parallel to the White Branch fault zone. Dextral slip on faults is predicted to accommodate this motion at the boundary but the components of this vector can also be broken down into velocity parallel (v_p = 1.04 mm/yr) and velocity normal (v_n = 0.4 mm/yr) motion (Figure 16) (Mark-Moser, 2018). The average summed horizontal extension rate across the White Branch fault zone calculated from the 1 km increment divisions of the fault zone is 0.4 ± 0.4 mm/yr and indicates the White Branch fault zone is capable of accommodating the v_n component of the slip vector calculated for the block boundary. However, the 1.04 mm/yr of fault-parallel motion that is predicted for the fault zone is not observed and must be accommodated on faults either not yet identified or by other means. Along the arc axis dextral shear is likely being accommodated through the White Branch fault zone extensional array which could explain the absence of lateral motion on the individual faults (Crider, 2001; Wesnousky et al., 2012). The Dilman Meadows fault zone is situated at a junction between the southern Oregon coast (southern Siletzia), eastern Oregon, and the Oregon Basin and Range tectonic domains in the McCaffrey et al. (2007) block model. The average extension rate for the fault zone is 0.5 ± 0.0 mm/yr and the extent to which these faults accommodate block rotation is unclear because of its position at the block boundaries.

It is likely that the same stresses that result in arc-parallel faulting also result in arc-parallel cinder cone alignment (Muffler et al., 2011; Deligne et al., 2016). The trends of the cinder cones in the Central Oregon volcanic field, ~8 km north of the White Branch fault zone, vary between N18°W – N11°W and N5°E – N7°E and the average strike of the faults in the White Branch fault zone are N25°E. The strike of the northern-most faults in the White Branch fault zone is more

northerly than faults further south which could be the result of the emplacement of feeder dikes ~200 to 300 m below the surface changing the stress orientations (Deligne et al., 2016). The faults at the White Branch Valley are likely not due to intrusive episodes like those recoded around South Sister volcano that produce little to no seismicity and last days to years and are separated by decades to centuries of quiescent periods (Dzurisin et al., 2006). Therefore, the faults in the White Branch fault zone are likely seismogenic and accommodate some fraction of Oregon forearc rotation in the High Cascades.

The Dilman Meadows fault zone is located south of the Mt. Bachelor volcanic chain and trenching evidence suggests colluviation followed by episodic motion on the Dilman Meadows fault indicating that some faults are seismogenic (Figure 17a). Graben-style faulting is apparent at the site, where sets of faults dip east and west cross the older outwash surface (Qgo_5) (Figure 17b). A fault in the eastern part of the outwash units displays scissor motion (Figure 17b), where across Qgo_5 the fault is dipping to the west and as it continues into Qgo_2 the dip direction changes to the east. A fault with its southern terminus in Qgo_5 is segmented to the north where north south oriented fissures strike parallel to the fault (Figure 17c) projecting towards a set of north-south aligned cinder cones. These faults may serve as a conduit for ascending magma or could be the result of changing stresses as magma ascends resulting in faulting (Figure 16).

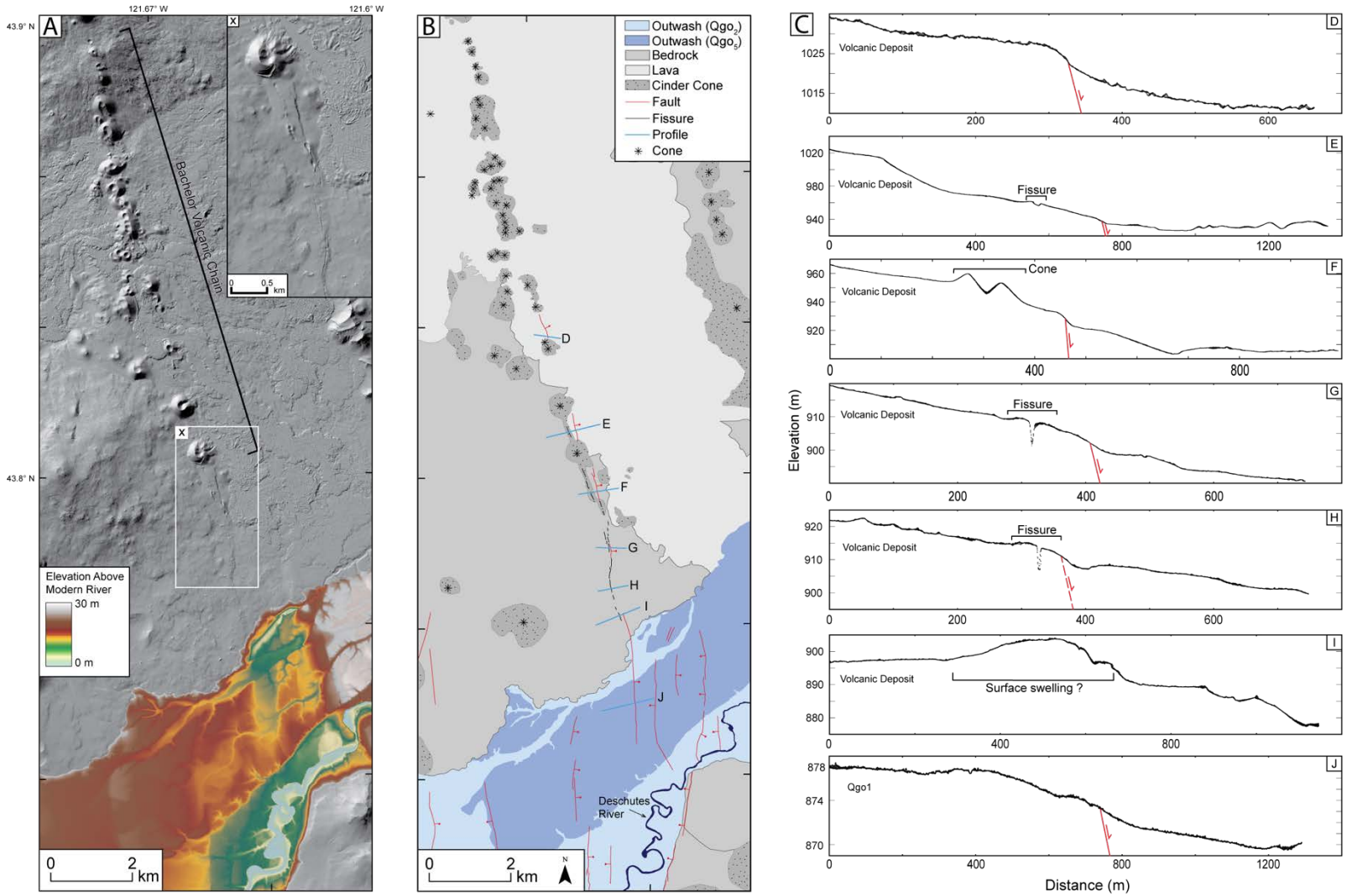

Figure 17: A): Uninterpreted hillshade of the Bachelor volcanic chain and the and the eastern Dilman Meadows fault zone. Elevation is colored by height above the modern Deschutes River. B): Simplified geologic map showing cinder cone alignment relative to the fault strike Profiles shown in C. C: Scarp profiles from north to south, showing relationship between fault, fissures, and cinder cones.

Conclusions

New mapping, cosmogenic nuclide dating, and scarp profiling in the Central Oregon Cascades provide new constraints on glaciation in the Pacific Northwest, and key insights for the mechanisms of Siletzia rotation and the resultant deformation of the central Oregon Cascades. From this work, we conclude the following:

i. Surficial geologic mapping based on bare-earth airborne lidar indicates three generations of glacial deposits on both sides of the Cascade crest. Dating of these landforms suggests glacial advances during both MIS 2 (~20 ka) and MIS 5 (~75 ka), and although not directly dated, possibly MIS 6, correlative to the 144 ± 14 ka Tahoe glaciation in the Sierra Nevada (Rood et al., 2011).

ii. Our cosmogenic ages suggest that glacial landforms correlate across the Cascade crest, and that this method works well for the dominantly basaltic andesite bedrock in the Oregon Cascades. We found that our ability to date individual moraine boulders ends at LGM age deposits, but dating older advances is possible using ^{3}He depth profiles.

iii. Offset measurements on the White Branch faults suggest observed deformation is all post-LGM deposition, despite multiple scarps crossing landforms that are at least MIS 5b in age. This pattern suggests either seismogenic quiescence or magmatic upwelling quiescence prior to the LGM. Faulting in the White Branch Valley area is bracketed in age by the deposition of LGM deposits and the most recent volcanism 1.6 ± 0.1 ka. The average strike of the White Branch fault zone is similar to alignment of cinder cones, likely because they share the same parent stresses.

iv. Faults cutting the surfaces in the White Branch fault zone accommodate primarily extension, with individual throws and slip rates being small, but, when summed, indicate regionally significant active deformation in this region.

	Average	Range
Summed slip rate	0.6 ± 0.5 mm/yr	0.3 – 2.1 mm/yr
Summed extension rate	0.4 ± 0.4 mm/yr	0.01 – 1.7 mm/yr

The White Branch fault zone could be connected to the Horse Creek fault at depth or could be a young fault zone that is accommodating new stresses that were unlike those accommodated by the Horse Creek fault.

v. The Dilman Meadows fault zone accommodates mostly extension, except in the case of the Dilman Meadows fault where we measured up to ~11 m of dextral offset. Evidence from trenching suggests that the faults are seismogenic, but in some locations, faults share along-strike continuity with fissures and are likely related to magma upwelling.

References

Ake, J., LaForge, R., and Hawkins, F., 2001, Probabilistic Seismic Hazard Analysis, Wickiup Dam: Deschutes Project, Central Oregon: Reclemation unpublished Seismotectonic Report 2000-04, p. 71 + appendixes.

Amidon, W.H., and Farley, K.A., 2011, Cosmogenic 3He production rates in apatite, zircon and pyroxene inferred from Bonneville flood erosional surfaces: Quaternary Geochronology, v. 6, p. 10–21, doi:10.1016/j.quageo.2010.03.005.

Anderson, R.S., Repka, J.L., and Dick, G.S., 1996, Explicit treatment of inheritance in dating depositional surfaces using in situ 10Be and 26Al: Geology, v. 24, p. 47, doi:10.1130/0091-7613(1996)024<0047:ETOIID>2.3.CO;2.

Axen, G.J., Fletcher, J.M., Cowgill, E., Murphy, M., Kapp, P., MacMillan, I., Ramos-Velázquez, E., Aranda-Gómez, J., and Juriquilla, C., 1999, Range-front fault scarps of the Sierra El Mayor, Baja California: Formed above an active low-angle normal fault? , p. 4.

Bacon, C.R., and Robinson, J.E., 2019, Postglacial faulting near Crater Lake, Oregon, and its possible association with the Mazama caldera-forming eruption: Geological Society of America Bulletin, v. 131, p. 19.

Balco, G., Stone, J.O., Lifton, N.A., and Dunai, T.J., 2008, A complete and easily accessible means of calculating surface exposure ages or erosion rates from 10Be and 26Al measurements: Quaternary Geochronology, v. 3, p. 174–195, doi:10.1016/j.quageo.2007.12.001.

Black, G.L., Priest, G.R., and Woller, N.N., 1988, Geologic map of the McKenzie Bridge quadrangle, Lane County, Oregon.: Geologic map series (Oregon. Department of Geology and Mineral Industries) ; GMS 48. cartographic, https://digital.osl.state.or.us/islandora/object/osl:231 (accessed February 2019).

Blard, P.-H. et al., 2015, An inter-laboratory comparison of cosmogenic 3 He and radiogenic 4 He in the CRONUS-P pyroxene standard: Quaternary Geochronology, v. 26, p. 11–19, doi:10.1016/j.quageo.2014.08.004.

du Bray, E.A., and John, D.A., 2011, Petrologic, tectonic, and metallogenic evolution of the Ancestral Cascades magmatic arc, Washington, Oregon, and northern California: Geosphere, v. 7, p. 1102–1133, doi:10.1130/GES00669.1.

Brocher, T.M., Wells, R.E., Lamb, A.P., and Weaver, C.S., 2017, Evidence for distributed clockwise rotation of the crust in the northwestern United States from fault geometries and focal mechanisms: Clockwise Rotation in the NW US: Tectonics, v. 36, p. 787–818, doi:10.1002/2016TC004223.

Chen, K., Avouac, J.-P., Aati, S., Milliner, C., Zheng, F., and Shi, C., 2020, Cascading and pulse-like ruptures during the 2019 Ridgecrest earthquakes in the Eastern California Shear Zone: Nature Communications, v. 11, p. 22, doi:10.1038/s41467-019-13750-w.

Couch, R., and Foote, R., 1985, The Shukash and La Pine Basins: Pleistocene Depressions in the Cascade RAnge of Central Oregon: Transactions American Geophysical Union, v. 66, https://agupubs.onlinelibrary.wiley.com/doi/abs/10.1029/EO066i046p00813.

Couch, R.W., Pitts, G.S., Gemperle, M., Braman, D.E., and Veen, C.A., 1982, Gravity Anomalies in the Cascade Range in Oregon: Structural and Thermal Implications:, https://www.oregongeology.org/pubs/ofr/O-82-09.pdf.

Crandell, D.R., and Miller, R.D., 1974, Quaternary stratigraphy and extent of glaciation in the Mt.Rainier region, Washington: U.S. Geol. Survey Prof. Paper, v. 847, p. 59.

Crider, J.G., 2001, Oblique slip and the geometry of normal-fault linkage: mechanics and a case study from the Basin and Range in Oregon: Journal of Structural Geology, v. 23, p. 1997–2009, doi:10.1016/S0191-8141(01)00047-5.

Darvill, C.M., 2013, Cosmogenic nuclide analysis: Geomorphological Techniques, p. 25.

Deligne, N.I., Conrey, R.M., Cashman, K.V., Champion, D.E., and Amidon, W.H., 2016, Holocene volcanism of the upper McKenzie River catchment, central Oregon Cascades, USA: GSA Bulletin, v. 128, p. 1618–1635, doi:10.1130/B31405.1.

Dunai, T.J., Stuart, F.M., Pik, R., Burnard, P., and Gayer, E., 2007, Production of 3He in crustal rocks by cosmogenic thermal neutrons: Earth and Planetary Science Letters, v. 258, p. 228–236, doi:10.1016/j.epsl.2007.03.031.

DuRoss, C.B., Bunds, M.P., Gold, R.D., Briggs, R.W., Reitman, N.G., Personius, S.F., and Toké, N.A., 2019, Variable normal-fault rupture behavior, northern Lost River fault zone, Idaho, USA: Geosphere, v. 15, p. 1869–1892, doi:10.1130/GES02096.1.

Dzurisin, D., Lisowski, M., Wicks, C.W., Poland, M.P., and Endo, E.T., 2006, Geodetic observations and modeling of magmatic inflation at the Three Sisters volcanic center, central Oregon Cascade Range, USA: Journal of Volcanology and Geothermal Research, v. 150, p. 35–54, doi:10.1016/j.jvolgeores.2005.07.011.

Egan, J., Staff, R., and Blackford, J., 2015, A high-precision age estimate of the Holocene Plinian eruption of Mount Mazama, Oregon, USA: The Holocene, v. 25, p. 1054–1067, doi:10.1177/0959683615576230.

England, P., and Wells, R.E., 1991, Neogene rotations and quasicontinuous deformation of the Pacific Northwest continental margin: Geology, v. 19, p. 978–981, doi:10.1130/0091-7613(1991)019<0978:NRAQDO>2.3.CO;2.

Fiebelkorn, R.B., Walker, G.W., MacLeod, N.S., McKee, E.H., and Smith, J.G., 1983, Index to K-Ar determinations for the State of Oregon: Isochron/West, no. 37, p. 3-60:

Gold, R., dePolo, C., Briggs, R., Crone, A., and Gosse, J., 2013, Late Quaternary Slip-Rate Variations along the Warm Springs Valley Fault System, Northern Walker Lane, California–Nevada Border: Bulletin of the Seismological Society of America, v. 103, p. 542–558, doi:10.1785/0120120020.

Gosse, J.C., and Phillips, F.M., 2001, Terrestrial in situ cosmogenic nuclides: theory and application: Quaternary Science Reviews, v. 20, p. 1475–1560, doi:10.1016/S0277-3791(00)00171-2.

Haddon, E.K., Amos, C.B., Zielke, O., Jayko, A.S., and Bürgmann, R., 2016, Surface slip during large Owens Valley earthquakes: SLIP DURING OWENS VALLEY EARTHQUAKES: Geochemistry, Geophysics, Geosystems, v. 17, p. 2239–2269, doi:10.1002/2015GC006033.

Hammond, W.C., 2005, Northwest Basin and Range tectonic deformation observed with the Global Positioning System, 1999–2003: Journal of Geophysical Research, v. 110, p. B10405, doi:10.1029/2005JB003678.

Hawkins, F.F., Foley, L.L., and LaForge, R.C., 1989, Seismo- tectonic study for Fish Lake and Fourmile Lake dams, Rogue River Basin Project, Oregon: U.S. Bureau of Reclamation Seismotectonic Report 89–3, 26 p.

Hayman, N.W., Knott, J.R., Cowan, D.S., Nemser, E., Sarna-Wojcicki, A.M., and Park, M., 2003, Quaternary low-angle slip on detachment faults in Death Valley, California: , p. 5.

Herrero-Bervera, E., Helsley, C., Sarna-Wojcicki, A., Lajoie, K., Meyer, C., McWilliams, M., Negrini, R., Turrin, B., Donnelly-Nolan, J., and Liddicoat, J., 1994, Age and Correlation of a paleomagnetic episode in the Western United States by Ar/Ar dating and tephrochronology: The Jamaica, Blake, or a new polarity episode: Journal of Geophysical Research, v. 99, p. 24091–24103.

Hildreth, W., 2007, Quaternary Magmatism in the Cascades -- Geologic Perspectives:, [http://pubs.usgs.gov/pp/pp1744/].

Ivy-Ochs, S., and Kober, F., 2008, Surface exposure dating with cosmogenic nuclides: Quaternary Science Journal, v. 57, p. 197–209.

Jefferson, A., Grant, G., and Rose, T., 2006, Influence of volcanic history on groundwater patterns on the west slope of the Oregon High Cascades: VOLCANIC HISTORY INFLUENCES GROUNDWATER: Water Resources Research, v. 42, doi:10.1029/2005WR004812.

Keach, R.W., Oliver, J.E., Brown, L.D., and Kaufman, S., 1989, Cenozoic active margin and shallow Cascades structure: COCORP results from western Oregon: GSA Bulletin, v. 101, p. 783–794, doi:10.1130/0016-7606(1989)101<0783:CAMASC>2.3.CO;2.

Licciardi, J.M., Clark, P.U., Brook, E.J., Elmore, D., and Sharma, P., 2004, Variable responses of western U.S. glaciers during the last deglaciation: Geology, v. 32, p. 81, doi:10.1130/G19868.1.

Lisiecki, L.E., and Raymo, M.E., 2005, A Pliocene-Pleistocene stack of 57 globally distributed benthic δ^{18}O records: PLIOCENE-PLEISTOCENE BENTHIC STACK: Paleoceanography, v. 20, p. n/a-n/a, doi:10.1029/2004PA001071.

Lyon, E., 2001, Late Quaternary geochronology and recent faulting along the eastern margin of the Shukash Basin, central Cascade range Oregon:

MacLeod, N.S., and Sherrod, D.R., 1988, Geologic evidence for a magma chamber beneath Newberry Volcano, Oregon: Journal of Geophysical Research, v. 93, p. 23.

MacLeod, N.S., and Sherrod, D.R., 1992, Reconnaissance geologic map of the west half of the Crescent 1 degree by 2 degrees quadrangle, central Oregon: U.S. Geological Survey Miscellaneous Investigations Series Map I-2215.

Mark-Moser, M., 2018, Role of the Sisters Fault Zone in the Separation of Siletzia from the Cascadia Backarc:, https://ir.library.oregonstate.edu/concern/graduate_thesis_or_dissertations/wd376226k?locale=en.

McCaffrey, R., King, R.W., Payne, S.J., and Lancaster, M., 2013, Active tectonics of northwestern U.S. inferred from GPS-derived surface velocities: PACIFIC NORTHWEST GPS: Journal of Geophysical Research: Solid Earth, v. 118, p. 709–723, doi:10.1029/2012JB009473.

McCaffrey, R., Qamar, A.I., King, R.W., Wells, R., Khazaradze, G., Williams, C.A., Stevens, C.W., Vollick, J.J., and Zwick, P.C., 2007, Fault locking, block rotation and crustal deformation in the Pacific Northwest: Geophysical Journal International, v. 169, p. 1315–1340, doi:10.1111/j.1365-246X.2007.03371.x.

Miller, M.M., Johnson, D.J., Rubin, C.M., Dragert, H., Wang, K., Qamar, A., and Goldfinger, C., 2001, GPS-determination of along-strike variation in Cascadia margin kinematics: Implications for relative plate motion, subduction zone coupling, and permanent deformation: Tectonics, v. 20, p. 161–176, doi:10.1029/2000TC001224.

Miller, R., and Markiewic, R., 2000, Shallow Seismic Reflection Survey At Wickiup Dam In Central Oregon: SAGEEP, 1245–1254 p.

Mix, A., 2001, Environmental processes of the ice age: land, oceans, glaciers (EPILOG): Quaternary Science Reviews, v. 20, p. 627–657, doi:10.1016/S0277-3791(00)00145-1.

Muffler, L.J.P., Clynne, M.A., Calvert, A.T., and Champion, D.E., 2011, Diverse, discrete, mantle-derived batches of basalt erupted along a short normal fault zone: The Poison Lake chain, southernmost Cascades: Geological Society of America Bulletin, v. 123, p. 2177–2200, doi:10.1130/B30370.1.

Numelin, T., Kirby, E., Walker, J.D., and Didericksen, B., 2007, Late Pleistocene slip on a low-angle normal fault, Searles Valley, California: Geosphere, v. 3, p. 163, doi:10.1130/GES00052.1.

Personius, S.F., 2002, Fault number 838, La Pine graben faults, in quaternary fault and fold database of the United States:, https:// earthquakes.usgs.gov/hazards/qfaults,.

Pezzopane, S.K., and Weldon, R.J., 1993, Tectonic role of active faulting in central Oregon: Tectonics, v. 12, p. 1140–1169, doi:10.1029/92TC02950.

Porter, S.C., and Swanson, T.W., 2008, 36Cl dating of the classic Pleistocene glacial record in the northeastern Cascade Range, Washington: American Journal of Science, v. 308, p. 130–166, doi:10.2475/02.2008.02.

Priest, G.R., 1990, Volcanic and tectonic evolution of the Cascade Volcanic Arc, central Oregon: Journal of Geophysical Research, v. 95, p. 19583, doi:10.1029/JB095iB12p19583.

Putkonen, J., and Swanson, T., 2003, Accuracy of cosmogenic ages for moraines: Quaternary Research, v. 59, p. 255–261, doi:10.1016/S0033-5894(03)00006-1.

Rood, D.H., Burbank, D.W., and Finkel, R.C., 2011, Chronology of glaciations in the Sierra Nevada, California, from 10Be surface exposure dating: Quaternary Science Reviews, v. 30, p. 646–661, doi:10.1016/j.quascirev.2010.12.001.

Sarna-Wojcicki, A., Meyer, C., Wan, E., and Soles, S., 1993, Age and correlation of tephra layers in Owens Lake drill core OL-92_1 and -2:

Savage, J.C., and Wells, R.E., 2015, Identifying block structure in the Pacific Northwest, USA: Journal of Geophysical Research: Solid Earth, v. 120, p. 7905–7916, doi:10.1002/2015JB012277.

Scarberry, K.C., Meigs, A.J., and Grunder, A.L., 2010, Faulting in a propagating continental rift: Insight from the late Miocene structural development of the Abert Rim fault, southern Oregon, USA: Tectonophysics, v. 488, p. 71–86, doi:10.1016/j.tecto.2009.09.025.

Scott, W.E., 1977, Quaternary glaciation and volcanism, Metolius River area, Oregon: Geological Society of America Bulletin, v. 88, p. 113, doi:10.1130/0016-7606(1977)88<113:QGAVMR>2.0.CO;2.

Scott, W.E., and Gardener, C.A., 1992, Geologic map of the Mount Bachelor volcanic chain and surrounding area, Cascade Range, Oregon: U.S. Geological Survey IMAP Report.

Sherrod, D.R., Taylor, E.M., Ferns, M.L., Scott, W.E., Conrey, R.M., and Smith, G.A., 2004, Geologic Map of the Bend 30- × 60-Minute Quadrangle, Central Oregon: , p. 49.

Simpson, R.W., and Cox, A., 1977, Paleomagnetic evidence for tectonic rotation of the Oregon Coast Range: , p. 5.

Speth, G.T., Amos, C.B., Amidon, W.H., Balco, G., Meigs, A.J., and Graf, S., 2018, Glacial chronology and slip rate on the west Klamath Lake fault zone, Oregon: GSA Bulletin, doi:10.1130/B31961.1.

Taylor, E.M., 1981, Central High Cascade roadside geology AND Road log for central High Cascade geology, Bend, Sisters, McKenzie Pass, and Santiam Pass, Oregon: U.S. Geological Survey Circular.

Taylor, E.M., 1990, Volcanic history and tectonic development of the Central High Cascade Range, Oregon: Journal of Geophysical Research, v. 95, p. 19611, doi:10.1029/JB095iB12p19611.

Thompson, S.C., Weldon, R.J., Rubin, C.M., Abdrakhmatov, K., Molnar, P., and Berger, G.W., 2002, Late Quaternary slip rates across the central Tien Shan, Kyrgyzstan, central Asia: SLIP RATES ACROSS THE KYRGYZ TIEN SHAN: Journal of Geophysical Research: Solid Earth, v. 107, p. ETG 7-1-ETG 7-32, doi:10.1029/2001JB000596.

Vadman, M.J., and Bemis, S.P., 2019, Active fault mapping and reconnaissance paleoseismic investigations in the La Pine graben, Oregon Cascades, USA: Geomorphology, v. 326, p. 6–16, doi:10.1016/j.geomorph.2018.10.003.

Waldien, T.S., Meigs, A.J., and Madin, I.P., 2019, Active dextral strike-slip faulting records termination of the Walker Lane belt at the southern Cascade arc in the Klamath graben, Oregon, USA: Geosphere, v. 15, p. 882–900, doi:10.1130/GES02043.1.

Walker, G.W., and Duncan, R.A., 1989, Geologic map of the Salem 1 degree x 2 degrees, quadrangle, western Oregon: U.S. Geological Survey Miscellaneous Investigations Series Map.

Weldon, R.J., Fletcher, D.K., Weldon, E.M., Scharer, K.M., and McCrory, P.A., 2003, An Update of Quaternary Faults of Central and Eastern Oregon:, https://pubs.usgs.gov/of/2002/of02-301/.

Wells, R.E., and Heller, P.L., 1988, The relative contribution of accretion, shear, and extension to Cenozoic tectonic rotation in the Pacific Northwest: Geological Society of America Bulletin, v. 100, p. 325–338, doi:10.1130/0016-7606(1988)100<0325:TRCOAS>2.3.CO;2.

Wells, R.E., Weaver, C.S., and Blakely, R.J., 1998, Fore-arc migration in Cascadia and its neotectonic significance: Geology, v. 26, p. 759, doi:10.1130/0091-7613(1998)026<0759:FAMICA>2.3.CO;2.

Wesnousky, S.G., Bormann, J.M., Kreemer, C., Hammond, W.C., and Brune, J.N., 2012, Neotectonics, geodesy, and seismic hazard in the Northern Walker Lane of Western North America: Thirty kilometers of crustal shear and no strike-slip? Earth and Planetary Science Letters, v. 329–330, p. 133–140, doi:10.1016/j.epsl.2012.02.018.

Zechar, J.D., and Frankel, K.L., 2009, Incorporating and reporting uncertainties in fault slip rates: Journal of Geophysical Research: Solid Earth, v. 114, doi:10.1029/2009JB006325.